Article (refereed) – Published version

Close, Sally E.; Naveira Garabato, Alberto C.; McDonagh, Elaine L.; King, Brian A.; Biuw, Martin; Boehme, Lars. 2013 Control of Mode and Intermediate Water Mass Properties in Drake Passage by the Amundsen Sea Low. *Journal of Climate*, 26 (14). 5102-5123. 10.1175/JCLI-D-12-00346.1

Control of Mode and Intermediate Water Mass Properties in Drake Passage by the Amundsen Sea Low

SALLY E. CLOSE AND ALBERTO C. NAVEIRA GARABATO

University of Southampton, National Oceanography Centre, Southampton, Southampton, United Kingdom

ELAINE L. MCDONAGH AND BRIAN A. KING

National Oceanography Centre, Southampton, Southampton, United Kingdom

MARTIN BIUW

Norwegian Institute for Nature Research, Tromsø, Norway

LARS BOEHME

Scottish Oceans Institute, St. Andrews, United Kingdom

(Manuscript received 13 June 2012, in final form 25 October 2012)

ABSTRACT

The evolution of the physical properties of Subantarctic Mode Water (SAMW) and Antarctic Intermediate Water (AAIW) in the Drake Passage region is examined on time scales down to intraseasonal, within the 1969–2009 period. Both SAMW and AAIW experience substantial interannual to interdecadal variability, significantly linked to the action of the Amundsen Sea low (ASL) in their formation areas. Observations suggest that the interdecadal freshening tendency evident in SAMW over the past three decades has recently abated, while AAIW has warmed significantly since the early 2000s. The two water masses have also experienced a substantial lightening since the start of the record. Examination of the mechanisms underpinning water mass property variability shows that SAMW characteristics are controlled predominantly by a combination of air–sea turbulent heat fluxes, cross-frontal Ekman transport of Antarctic surface waters, and the evaporation–precipitation balance in the Subantarctic zone of the southeast Pacific and Drake Passage, while AAIW properties reflect air–sea turbulent heat fluxes and sea ice formation in the Bellingshausen Sea. The recent interdecadal evolution of the ASL is consistent with both the dominance of the processes described here and the response of SAMW and AAIW on that time scale.

1. Introduction

The water masses formed in the Southern Ocean are exported globally and constitute a substantial proportion of the total ocean volume. Subantarctic Mode Water (SAMW) and Antarctic Intermediate Water (AAIW) are integral to the upper cell of the meridional overturning circulation and contribute importantly to balancing the southward flow of North Atlantic Deep Water (Sloyan and Rintoul 2001; Ganachaud and Wunsch 2000; Lumpkin and Speer 2007). The SAMW and AAIW exported from the Southern Ocean ventilate much of the global subtropical pycnocline (McCartney 1982; Hanawa and Talley 2001) and play a key role in the transport and storage of heat, freshwater, and biogeochemical tracers imprinted on the water masses during their production (Sabine et al. 2004; Sarmiento et al. 2004). There is thus much interest in determining how the properties of the SAMW and AAIW entering the ocean interior reflect climatic changes in their formation regions, yet progress is hindered by our limited understanding of the climatic controls of SAMW and AAIW production and the mechanisms by which such controls are exerted.

Corresponding author address: Sally E. Close, Centre de Recherches sur la Terre et le Climat Georges Lemaître, Earth and Life Institute, Université catholique de Louvain, Place Louis Pasteur 3, 1348 Louvain-la-Neuve, Belgium.
E-mail: sally.close@uclouvain.be

DOI: 10.1175/JCLI-D-12-00346.1

SAMW is believed to be formed on the equatorward edge of the Antarctic Circumpolar Current (ACC) in several areas of the south Indian and South Pacific Oceans during winter as a result of the seasonal deepening of the mixed layer, and is characterized by low potential vorticity and high oxygen concentration (McCartney 1977; Aoki et al. 2007; Sallée et al. 2006). It has relatively uniform properties, with temperatures in the range of approximately 4°–15°C and salinities of 34.2–35.8 that vary regionally (Hanawa and Talley 2001). A key facet of the SAMW formation process is the regionalized wintertime extraction of buoyancy from the upper ocean. Two major mechanisms have been suggested to effect this buoyancy loss: air–sea turbulent heat fluxes (McCartney 1977; Bindoff and Church 1992; Johnson and Orsi 1997) and the wind-driven Ekman transport of relatively dense waters across the Subantarctic Front (SAF; Rintoul and England 2002). In practice, these two regional processes may play roles of comparable significance, with the prevalence of one or the other being subject to substantial spatiotemporal variability (Naveira Garabato et al. 2009).

While the advent of widespread remote observing platforms such as the Argo float network has permitted the formation of SAMW to be documented (Aoki et al. 2007), considerable incertitude persists regarding the mechanisms by which AAIW is produced. A contribution of subduction of Winter Water along isopycnals at the Polar Front (PF) has been highlighted by a number of studies (e.g., Meredith et al. 1999; Naveira Garabato et al. 2001, 2009; Santoso and England 2004; Sallée et al. 2010), yet others emphasize the role of the overlying SAMW in setting AAIW properties in the southeast Pacific (Talley 1996; McCartney 1977; Herraiz-Borreguero and Rintoul 2011). Formation process considerations aside, AAIW is characterized by a distinctive salinity minimum occurring at the core of the water mass. AAIW enters the oceanic pycnocline at the SAF and flows equatorward at a depth of around 1000 m. Reflecting this circulation pattern, the salinity minimum is at its coldest and freshest at the SAF and gradually warms and salinifies equatorward (Talley 1996).

The pycnocline layers of the global ocean ventilated by SAMW and AAIW have been suggested to have experienced substantial variability in recent decades, on time scales up to the multidecadal length of the observational record. A circumpolar-mean warming of the depth range occupied by SAMW and AAIW in the Southern Ocean by about 0.17°C on isobaric surfaces has been reported between the 1950s and 1990s that approximately doubles the global-average warming trend within the same depth range and period (Gille 2002, 2008; Levitus et al. 2000, 2009). This has been accompanied by an interdecadal circumpolar-mean freshening of the upper kilometer of the Southern Ocean of approximately 0.04 yr^{-1} on isopycnal surfaces between the 1960s and 2000s (Böning et al. 2008; von Schuckmann et al. 2009). Both of these changes exhibit broad consistency with those reported to have occurred in the SAMW and AAIW density classes of the Indian Ocean and Pacific subtropics, where the water masses warmed by up to 0.5°C and freshened by ~0.02 between the 1960s and 1990s (Bindoff and Church 1992; Wong et al. 1999; Bindoff and McDougall 2000; Bindoff et al. 2007), and across the South Atlantic, where SAMW and AAIW experienced a freshening of up to 0.2 between the 1950s and 1990s (Curry et al. 2003). A common interpretation of this collection of interdecadal changes in SAMW and AAIW properties is that they form part of a global-scale pattern of warming and freshening (salinification) of mode and intermediate waters of subpolar (subtropical) origin in recent decades (Durack and Wijffels 2010; Wong et al. 2001; Johnson and Orsi 1997; Church et al. 1991). As highlighted by the Intergovernmental Panel on Climate Change Fourth Assessment Report (Bindoff et al. 2007, and references therein) and, more recently, by Durack et al. (2012), this pattern is a plausible major feature of the oceanic response to the global atmospheric warming and acceleration of the atmospheric hydrological cycle that are thought to have occurred in the last several decades and that are consistent with model projections of climate change in rising greenhouse gas scenarios.

Despite the attractive simplicity of the above patterns and interpretation of SAMW and AAIW property changes, our mechanistic understanding and even the robustness of these large-scale variations have been called into question by several studies. For example, Bryden et al. (2003) and McDonagh et al. (2005) report that, between 1987 and 2002, the warming and freshening tendencies experienced by the upper pycnocline of the subtropical south Indian Ocean prior to the 1990s underwent a reversal, while Schneider et al. (2005) reveal a similar transition in the AAIW of the subtropical South Pacific. Studies examining time series of SAMW and AAIW properties in their formation regions contribute further to this disparate picture, with Herraiz-Borreguero and Rintoul (2010) finding substantial interannual variations in SAMW properties south of Tasmania over the period 1991–2007 but no significant decadal-scale tendencies. The role of mesoscale features in rapidly effecting substantial intra- and interannual variability in SAMW properties was emphasized in this study, and linked to a local manifestation of the southern annular mode (SAM). A similar level of complexity in the observed variability of SAMW and AAIW characteristics was noted by Naveira Garabato et al. (2009),

who examined a 36-yr record of water mass properties in the mode and intermediate water formation region spanning the southeast Pacific and Drake Passage. SAMW was found to experience a ~30-yr oscillation in its thermohaline characteristics (with amplitude of ~0.3°C in temperature and ~0.04 in salinity) between the late 1960s and 2005 and AAIW to undergo a net freshening of ~0.05 in the same period. The modulation of interannual to interdecadal variability in SAMW and AAIW properties by the SAM, El Niño–Southern Oscillation (ENSO), and the closely related Pacific decadal oscillation was highlighted by those authors, although the mechanisms of atmospheric and cryospheric forcing via which the major climatic modes control mode and intermediate water properties in the region were only tangentially explored.

The complex picture of variability revealed by the preceding studies suggests that, if the causes of the large-scale warming and freshening of SAMW and AAIW that are apparent across much of the subtropical ocean are to be established, both the mechanisms responsible for setting water mass properties and the climatic controls of those mechanisms must be understood. Here, we address this problem in the region of SAMW and AAIW formation in and adjacent to Drake Passage, one of the most densely sampled sectors of the Southern Ocean. High spatiotemporal data coverage is crucial for accurate quantification of both the changes in water mass properties on time scales of interest (down to interannual) and of the errors incurred by undersampling variability on shorter time scales. Section 2 describes the range of data types that are combined in this study to obtain a comprehensive coverage of the region, and outlines the method of analysis. Section 3 characterizes the variability of regional SAMW and AAIW properties on interannual to interdecadal time scales. The mechanisms responsible for driving this variability are investigated in section 4. Our key result is that changes in the characteristics of both water masses are primarily controlled by variability in the atmospheric circulation associated with the Amundsen Sea low, with this control being exerted by distinct mechanisms for each water mass (this key result is synthesized schematically in Fig. 16).

TABLE 1. Drake Passage sections analyzed in this study, updated from Naveira Garabato et al. (2009).

Section	Vessel (citation)	Date of occupation
SR1	*Thomas Washington* (Boyer et al. 2009)	20–27 Jan 1969
SR1W	*Hudson* (Boyer et al. 2009)	5–15 Feb 1970
SR1	*Melville* (Boyer et al. 2009)	27 Feb–7 Mar 1975
SR1	*Melville* (Boyer et al. 2009)	16–22 Mar 1975
SR1	*Thompson* (Boyer et al. 2009)	26 Feb–3 Mar 1976
SR1	*Melville* (Boyer et al. 2009)	19 Jan–3 Feb 1977
SR1	*Yelcho* (Boyer et al. 2009)	15–20 Apr 1979
SR1	*Atlantis* (Boyer et al. 2009)	19 Jan–13 Feb 1980
SR1W	*Meteor* (Boyer et al. 2009)	24 Jan–1 Feb 1990
SR1b	*James Clark Ross* (Bacon and Cunningham 2005)	21–26 Nov 1993
SR1b	*James Clark Ross* (Bacon and Cunningham 2005)	15–21 Nov 1994
SR1b	*Hespérides* (Boyer et al. 2009)	15–19 Feb 1996
SR1b	*James Clark Ross* (Bacon and Cunningham 2005)	15–20 Nov 1996
SR1b	*James Clark Ross* (Bacon and Cunningham 2005)	29 Dec 1997–7 Jan 1998
SR1b	*Hespérides* (Boyer et al. 2009)	13–18 Feb 1998
SR1b	*Hespérides* (Boyer et al. 2009)	8–14 Dec 1998
SR1W	*James Clark Ross* (Bacon and Cunningham 2005)	18–26 Mar 1999
SR1b	*James Clark Ross* (Bacon and Cunningham 2005)	12–17 Feb 2000
SR1b	*James Clark Ross* (Cunningham 2001)	22–28 Nov 2000
SR1b	*James Clark Ross* (Bacon 2002)	20–26 Nov 2001
SR1b	*James Clark Ross* (Bacon 2003)	27 Dec 2002–1 Jan 2003
SR1b	*James Clark Ross* (Hawker et al. 2005)	11–15 Dec 2003
SR1b	*James Clark Ross* (Sparrow and Hawker 2005)	2–8 Dec 2004
SR1b	*James Clark Ross* (Stansfield and Meredith 2008)	7–12 Dec 2005
SR1b	*James Clark Ross* (Williams et al. 2008)	7–15 Dec 2006
SR1b	*James Clark Ross* (Quartly and Venables 2010)	29 Nov–5 Dec 2007
SR1b	*James Clark Ross* (Quartly 2010)	12–18 Dec 2008
SR1W	*James Cook* (McDonagh 2009)	3–18 Feb 2009
SR1b	*James Cook* (McDonagh 2009)	19–26 Feb 2009

2. Data and methods

a. In situ data

Historical hydrographic cruise data, updated from the dataset used by Naveira Garabato et al. (2009) and listed in Table 1, are combined with Argo observations (covering the period February 2002–October 2009) and measurements collected using seal-mounted sensors as part of the Southern Elephant Seals as Oceanographic Samplers (SEaOS; 2004–05) program (Boehme et al. 2008b, 2009; Charrassin et al. 2008; Biuw et al. 2007). The dataset encompasses the period 1969–2009, spanning the time (1993–2009) over which quasi-annual repeat hydrographic transects have been occupied in Drake Passage. A map showing the data coverage in the area surrounding Drake Passage is shown in Fig. 1, where the green outline indicates the area used in evaluating the properties of SAMW and AAIW in this

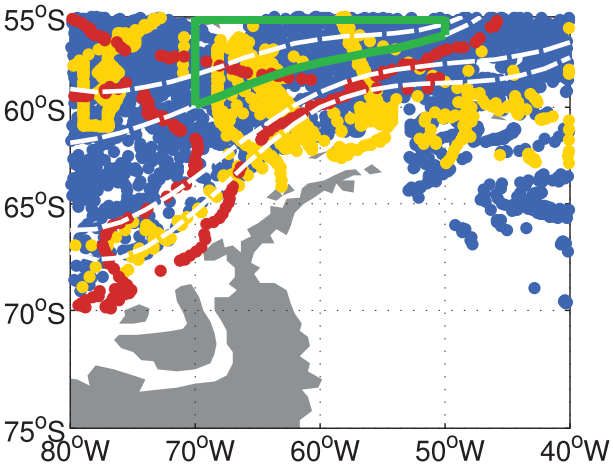

FIG. 1. Map of data availability in the study region, colored by data type. Blue dots indicate Argo data, red dots show sea seal-mounted sensor data, and yellow dots denote ship-based observations. The green triangle indicates the approximate area over which water mass properties are estimated in this work. Mean positions of the major fronts as estimated from dynamic topography are shown by white dashed lines (from top to bottom: Subantarctic Front, Polar Front, southern ACC Front, and southern boundary).

work. The range is bounded to the north at 55°S in order to exclude short-term variability associated with the subtropical gyre. The SAF forms the southern boundary of SAMW, while the PF delineates the southern boundary of AAIW. All Argo profiles with quality flags less than "good" or with known pressure problems were removed. The θ–S properties of all profiles were examined, and any profiles which showed significant deviation from their neighboring profiles [>two standard deviations on neutral density surfaces within 5° longitude and 0.03 dynamic meter (1 dyn m = 10 m^2 s^{-2}) bins] were also discarded.

b. Auxiliary data

A number of additional datasets are employed in the investigation of the mechanisms responsible for forcing variability. National Oceanic and Atmospheric Administration optimum interpolation sea surface temperature (SST) monthly-mean data are used, combining in situ and satellite measurements (available from http://www.esrl.noaa.gov/psd/data/gridded/data.noaa.oisst.v2.html). To examine links between water mass properties and the cryosphere, National Snow and Ice Data Center sea ice data retrieved from the *Nimbus-7* Scanning Multichannel Microwave Radiometer and Defense Meteorological Satellite Program *F-13* and *F-17* Special Sensor Microwave Imager passive microwave measurements are analyzed (Cavalieri et al. 2008). In addition to these observation-based products, two atmospheric reanalysis products are considered: the European Centre for Medium-Range Weather Forecasting (ECMWF) Interim Reanalysis (ERA-Interim; Dee et al. 2011) and the National Centers for Environmental Prediction–National Center for Atmospheric Research (NCEP–NCAR) reanalysis (Kalnay et al. 1996). From these two products, monthly-mean fields of momentum and heat fluxes and net precipitation are used to analyze the role of wind stress, air–sea turbulent heat flux, and changes in the evaporation–precipitation (E–P) balance in driving variability in water mass properties. In addition to the above data sources, indices are used to characterize the behavior of ENSO and the SAM over the period under consideration. The bivariate ENSO time series (BEST) (Smith and Sardeshmukh 2000) is used to characterize ENSO (available from http://www.cdc.noaa.gov/people/cathy.smith/best/), while SAM is described using the station-based index of Marshall (2003) (available from http://www.nerc-bas.ac.uk/icd/gjma/sam.html).

c. Methods

Previous studies show that the fronts of the ACC meander over large distances on time scales as short as a few days (Sokolov and Rintoul 2002, 2009; Boehme et al. 2008a,b). A comparison of observations at a given geographic (i.e., latitude–longitude) point thus cannot be assumed to provide a clear description of the variability of individual water masses, due to the possibility of sampling different hydrographic zones in consecutive profiles at the same location. To minimize the variability associated with this issue, dynamic height, rather than latitude, is used as the meridional coordinate in this work. The results obtained show minimal dependence on the choice of reference pressure levels, and dynamic height is thus calculated at 500 dbar relative to 1500 dbar, with the deeper bound being chosen to maximize data availability. The shallow bound is determined using a mixed layer depth–based criterion: 97% of profiles have a (nonwinter) mixed layer depth of <500 m, and thus this value is selected to balance the preference of excluding as much as possible of the variability associated with the mixed layer with that of maximizing availability of data.

A further problem to be addressed is the isolation and exclusion of variability associated with the temporally evolving spatial distribution of the data. The Southern Ocean may exhibit a substantial spatial (particularly cross stream) structure in the distribution of thermohaline properties, both on isobaric and (less so) on isopycnal surfaces. This spatial variability may thus bias calculations of temporal changes in water mass properties in an analysis based on averaging over a given area, if the spatial distribution of the data is itself variable in time. To compensate for this, a gravest empirical mode approach (Sun and Watts 2001) is adopted and "standard"

background fields of temperature, salinity, and pressure are calculated: the data are gridded to a 0.01 kg m^{-3} neutral density grid in the vertical and binned in 0.03 dyn m intervals in the cross-stream direction. Longitudinal dependence is minimal over the interval 50°–70°W, and hence not accounted for. Cubic splines are then fitted to the bin means on neutral density levels, yielding sets of functions describing the background conditions. Subtraction of these estimates from the observed data leads to a greatly reduced spatial dependence, thus providing a spatially coherent estimate of water mass property anomalies.

To enable calculation of bulk water mass properties, neutral density and dynamic height ranges associated with SAMW and AAIW are defined. Through detection of profiles containing the salinity maximum associated with the base of the SAMW layer, the SAF is determined to be associated with the dynamic height value $\phi_{500–1500} = 0.70$ dyn m. Similarly, through identification of the sharp transition in upper-ocean water mass properties associated with the PF, a value of $\phi_{500–1500} = 0.54$ dyn m is identified for this feature. SAMW is thus expected to be present in profiles with $\phi_{500–1500} > 0.70$ dyn m, while AAIW is found in profiles with $\phi_{500–1500} > 0.54$ dyn m. Neutral density ranges are determined by locating the salinity maximum associated with the base of the SAMW layer and the salinity minimum associated with the core of AAIW in all profiles selected by the dynamic height ranges defined above and taking the mean value ±1 standard deviation. This yields ranges $27.1 < \gamma_n < 27.23$ kg m^{-3} for SAMW and $27.23 < \gamma^n < 27.5$ kg m^{-3} for AAIW. Water mass properties for SAMW and AAIW are then calculated by binning the data by season, selecting appropriate dynamic height and neutral density ranges, and averaging the anomaly data for that season (with all data lying in the top 200 dbar being excluded from the analysis to minimize the effects of variability associated with the mixed layer). The analysis has been repeated on both neutral density and pressure surfaces, facilitating examination of heave and density-compensating phenomena.

Both instrumental error and error due to undersampling are considered in the calculation of uncertainties associated with the seasonal estimates. Various data sources are combined in this work, and these have different instrument errors, with ship-based CTD data expected to have the highest accuracy. Where various data sources are combined to calculate a seasonal mean, the accuracy of the instrument with the highest error is used (e.g., where ship-based CTD data and Argo data are combined, the accuracy of the Argo data is used as the error). The expected accuracies of the various data sources are given in Table 2.

TABLE 2. Instrument-specific errors associated with different data sources. SRDL is Satellite Relay Data Logger.

Data source	Temperature error (°C)	Salinity error	Pressure error (dbar)	Citation
Argo	0.005°	0.01	5	Carval et al. 2008
Ship-based CTD	0.002°	0.002	3	King et al. 2001
CTD-SRDL	0.02°	0.02	5	Boehme et al. 2008a

To estimate the uncertainty due to undersampling, the water mass variability analysis described above is repeated using only a subset of the total available data. For a season where N observations are available for a given water mass, for each element n in the set of integers $\mathbb{Z}_N$, n profiles are randomly selected from all available observations. These n profiles are then averaged over the water mass' assigned neutral density range to give a mean value for the season as in the analysis described above, thus recreating the time series using fewer observations than are available. Fifty iterations of this subsampling are performed, and the differences between the values obtained using all available observations and the values obtained using only n observations found. An exponential fit is conducted, yielding an estimate of uncertainty as a function of the number of available observations (full details are given in Close 2011). The further effects of spatial and temporal bias within this subsampling were found to be negligible compared to the error due to limited data availability. The simpler analysis in which no spatial dependence is accounted for is hence applied, thus maximizing data availability. These error estimates are combined in quadrature with the instrumental error to give the total uncertainty.

3. Variability of SAMW and AAIW properties

SAMW experiences substantial interdecadal tendencies in both salinity and pressure (Fig. 2), with total differences of approximately 0.05 and 200 dbar between the 1990s and late 2000s (cf. the mean interdecadal variability of 0.13° ± 0.08°C, 0.019 ± 0.008, and 44 ± 26 dbar). Temperature shows strong interannual variability but has no comparable interdecadal signal to that undergone in salinity and pressure. The salinity trend appears to undergo a reversal after approximately 2005, and a linear regression suggests a mean freshening of 0.004 yr^{-1} between 1990 and this time, consistent with previous analyses (e.g., Naveira Garabato et al. 2009). The most

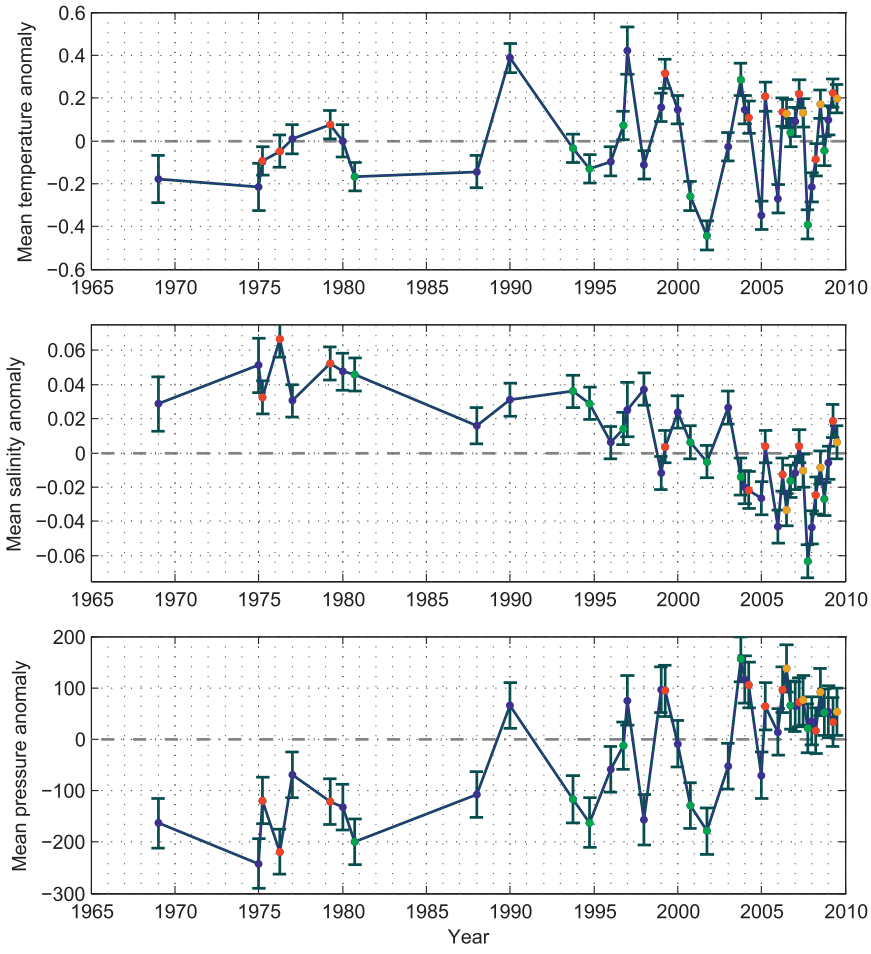

FIG. 2. SAMW anomaly properties (top) θ and (middle) salinity averaged on pressure surfaces and (bottom) pressure anomaly properties averaged on neutral density surfaces, over the $\phi_{500-1500} > 0.7$ dyn m and $27.1 < \gamma_n < 27.23$ kg m^{-3} ranges. Green points indicate spring [September–November (SON)], blue refers to summer [December–February (DJF)], red indicates autumn [March–May (MAM)], and yellow denotes winter [June–August (JJA)].

recent data suggest that this trend has recently been abating, with the post-2005 data indicating a stabilization in SAMW salinity. A linear regression of all available data over the period 2005–10 yields a salinifying trend of 0.003 yr^{-1}. This trend is, however, reduced to 0.002 yr^{-1} if only spring–summer data are utilized, indicating that increased seasonal data availability in the latter years of the time series may affect the estimate. The change in temperature is less robust than that in salinity: linear regression yields a warming of 0.04°C yr^{-1} over the period 2005–10, with the difference between the 2000–05 and 2005–10 period means suggesting an increase in temperature of 0.11°C between the two pentads. However, as for salinity, this is sensitive to the inclusion of seasonal data, and, considered in isolation, the spring–summer data suggest negligible change in temperature.

A further striking feature of the SAMW analysis is the significant deepening trend evident between the early 1990s and 2010, suggesting a change in the stratification of the upper water column in this region. This is believed to be largely unrelated to the phenomena described in this work, the relevant mechanism being discussed by Close and Naveira Garabato (2012).

The amplitude of interannual variability exhibited by SAMW remains approximately constant throughout the time series. Using only data from austral spring–summer, the seasons with the greatest data availability, yields mean interannual variability of 0.02 ± 0.01 in salinity and 0.25° ± 0.14°C in potential temperature. The maximum interannual variability observed is 0.05 ± 0.02 and 0.52° ± 0.13°C, approximately twice the mean interannual variability. In contrast, interannual variability in pressure appears to decrease in magnitude, with

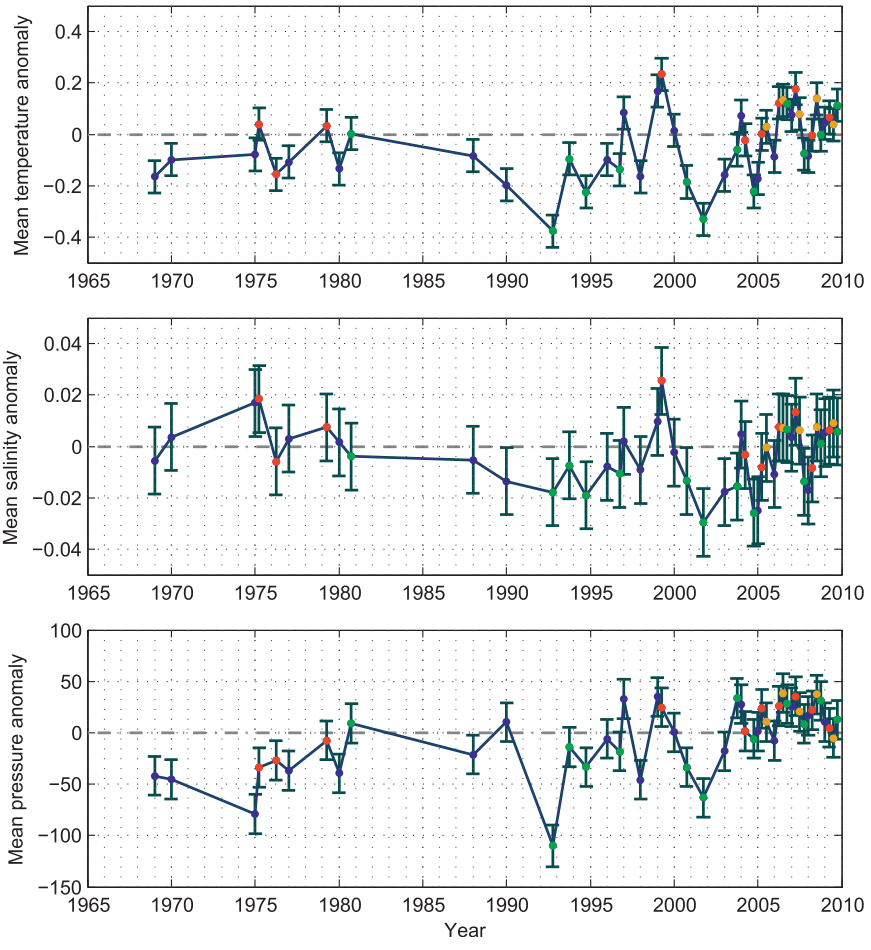

FIG. 3. As in Fig. 2, but for AAIW averaged over the $0.7 \geq \phi_{500\text{–}1500} > 0.54$ dyn m and $27.23 < \gamma_n < 27.5$ kg m^{-3} ranges.

a mean value of 131 ± 6 dbar over the period 1995–2005, reducing to 59 ± 5 dbar over 2005–10.

Interdecadal changes in AAIW are considerably more subtle than those in SAMW (Fig. 3). However, there is again some evidence of persistent change over 2000–10: the time series indicate increases in temperature and pressure anomaly over this period, with a lesser increase also evident in salinity. These changes are more significantly affected by the inclusion of seasonal data than those in SAMW, with temperature showing a mean total warming of 0.1°C between 1990–2000 and 2000–2010 if all data are included but a negligible difference if only spring–summer data are considered. A deepening trend (2.8 ± 0.7 dbar yr^{-1} over 1990–2010) is again evident in the pressure analysis.

To synthesize the above results, measurements from the repeat SR1b hydrographic line lying to the north of the SAF are grouped pentannually and the mean θ–S properties are calculated (Fig. 4, top). The averaged data reflect the salinity variability seen in the SAMW time series, with the density range 27.1–27.23 kg m^{-3} showing a monotonic freshening of approximately 0.05 between the pre-1993 mean and the 2005–09 mean. The data also reflect the abatement of the freshening trend between 2000–05 and 2005–09, with little associated change in temperature throughout the density range. This further suggests a decrease in density of the SAMW layer, with the base of the layer being shifted across isopycnal surfaces from 27.23 ± 0.02 kg m^{-3} in the pre-1993 average to 27.18 ± 0.02 kg m^{-3} in the 2005–09 mean. The decrease in SAMW density is also evident in the potential vorticity (PV) of the water mass (Fig. 4, bottom). The PV minimum occurs in lighter density classes in later years (with the minimum again shifting from 27.23 ± 0.02 kg m^{-3} in the pre-1993 average to 27.18 ± 0.02 kg m^{-3} in the most recent average, as in the θ–S diagram), suggesting subduction of lighter surface waters.

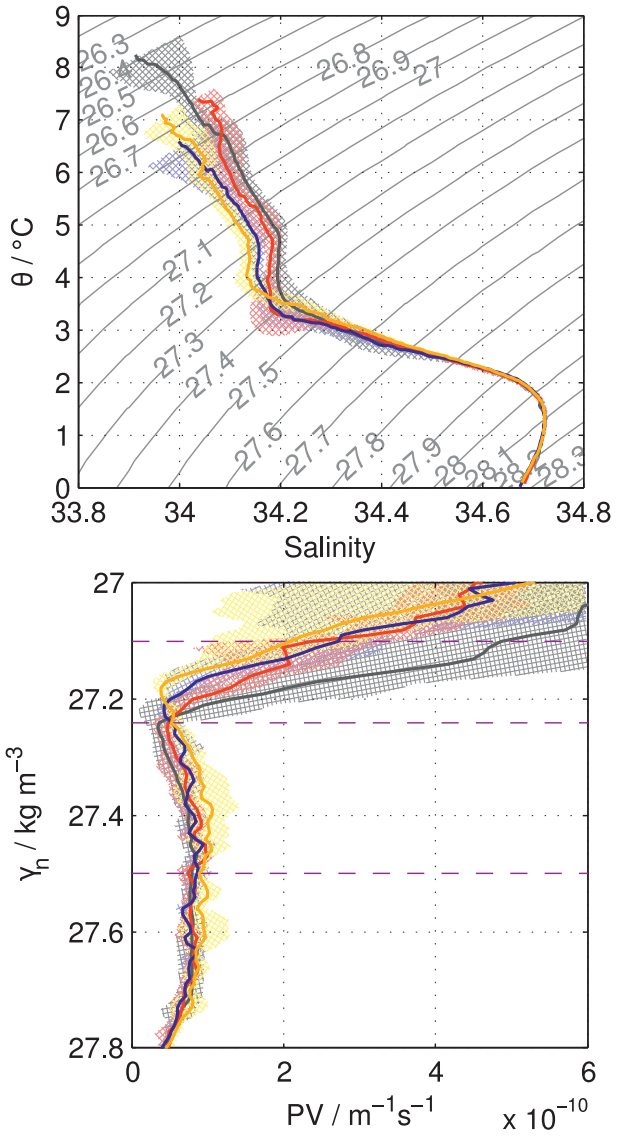

FIG. 4. (top) A θ–S diagram showing water mass properties north of the SAF at the northern edge of the SR1b section, averaged on neutral density surfaces and grouped pentannually. The dark gray line shows the pre-1993 average, the red line corresponds to 1994–99, the blue line shows 2000–04, and the yellow line indicates the 2005–09 mean. Hatched areas show the standard deviation envelopes, with the same color scheme. (bottom) Corresponding mean PV profiles for the periods above. Data are averaged over the same area, on neutral density surfaces, and with the same color scheme.

Figure 4 also suggests a consistent scenario of change in AAIW with that apparent in the time series analysis, with the AAIW density range being warm and saline in the pre-1993 analysis, before cooling, and shifting to a denser state between 1994 and 2005, prior to a warming of the salinity minimum and recovery in density between 2005 and 2009. These data further support the idea that changes in SAMW have been predominantly

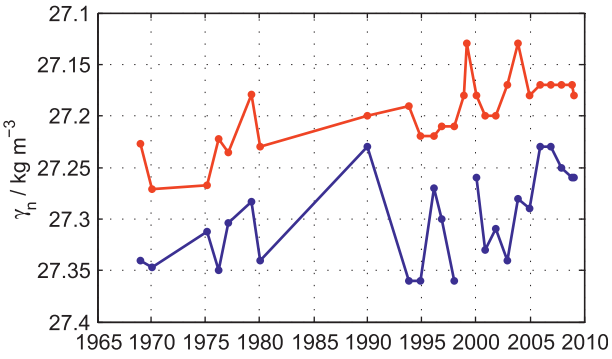

FIG. 5. Time series of neutral density at the salinity maximum of the SAMW layer (red) and at the salinity minimum at the core of AAIW (blue) over the period 1969–2009. The break in the blue line around 1999 corresponds to the disappearance of the salinity minimum associated with a 1–2-yr cessation in AAIW ventilation (see Naveira Garabato et al. 2009).

driven by changes in salinity; while those in AAIW have been predominantly driven by temperature variations.

The notion of a recent interannual freshening of SAMW and a warming of AAIW is further endorsed by the decreasing neutral density of the salinity maximum (minimum) at the base of the SAMW (core of the AAIW layer) (Fig. 5), again calculated from the SR1b repeat hydrography and, as for the water mass analysis above, excluding the mixed layer. Both water masses exhibit a trend toward a lighter state between the mid-1990s and 2009, with SAMW showing a lightening trend throughout the time series. These decreases are consistent with the previously mentioned freshening/warming tendencies and, as with the pressure data, are suggestive of stratification changes in the upper part of the water column.

While the accuracy of the earliest (pre-1990) data in the time series cannot be precisely determined, the interdecadal tendencies discussed are robust even bearing this in mind, with the most significant changes occurring in the post-1990 period. Considering data from all seasons, AAIW exhibits a post-1990 warming trend of 0.014 ± 0.009°C yr^{-1} that is statistically significant at the 95% level, while neither the full record AAIW trend of $0.003° \pm 0.003$°C yr^{-1} nor pre-1990 trend of $0.008° \pm 0.009$°C yr^{-1} is significant (at the 90% level). Equally, the SAMW freshening trend is statistically significant at the 95% level both over the full record and over the post-1990 period, with trends of $(-1.8 \pm 0.5) \times 10^{-3}$ and $(-2.8 \pm 1.4) \times 10^{-3}$, respectively, while the pre-1990 regression indicates negligible change, with a trend of $(-0.7 \pm 1.9) \times 10^{-3}$ that is not significant at the 90% level. Constructing the time series using either solely ship-based or solely non-ship-based data results in a time series that retains the same major features over

the periods where the relevant data are available (Close 2011).

4. Driving mechanisms of the observed variability

Atmospheric forcing plays a critical role in determining SAMW and AAIW properties, whether this influence is exerted through air–sea turbulent heat fluxes, Ekman transport, or modulation of sea ice coverage. A key feature of the atmospheric circulation in the western part of the study region is the Amundsen Sea low (ASL). This is a center of cyclonic atmospheric flow, lying in the region of the Amundsen–Bellingshausen sector, which is believed to arise as a result of the Antarctic orography (Baines and Fraedrich 1989). The ASL has been suggested both to experience significant modulation by the major atmospheric modes (Chen et al. 1996; Simmonds and King 2004) and to have intensified in recent decades (Turner et al. 2009). It has been suggested that the Pacific–South America (PSA) teleconnection, which plays a prominent role in transmitting ENSO events to high southern latitudes (Carleton 2003), may be significant in modulating the ASL. (The PSA is a standing wave train of atmospheric anomalies that originates in the western equatorial Pacific and manifests in a series of high and low pressure systems crossing southeastward across the South Pacific toward the southwest Atlantic–Weddell Sea.) In the southeast Pacific, the PSA can act to significantly modify the ASL by inducing positive sea level pressure anomalies in the Amundsen–Bellingshausen sector during El Niño events and negative sea level pressure anomalies during La Niña episodes (Yuan and Li 2008). The induced pressure anomalies can modify the shape and/or intensity of the pressure field adjacent to the ASL, with the manifestation being dependent upon the relative location of the anomaly. The ASL may also experience forcing by the SAM: Fogt et al. (2011) observe that the SAM becomes more zonally asymmetric when occurring in strong antiphase with ENSO. This asymmetric component occurs over the Amundsen–Bellingshausen sector and may thus also drive either an enhancement or weakening of the ASL, depending on the sign of the two modes. Both the proximity of the ASL to the study area and its significant influence on the atmospheric circulation suggest it as a likely influence on the mechanisms that may drive water mass variability in the study region, and its role in effecting change in the SAMW and AAIW formation regions will be considered below.

As discussed previously, SAMW has been suggested to be formed in winter by deep convection on the equatorward flank of the SAF (McCartney 1977), whereas AAIW has been proposed to experience significant ventilation by Winter Water, the remnant winter mixed layer south of the PF (Meredith et al. 1999). The summertime properties of SAMW and AAIW might thus be expected to reflect the surface properties of their formation areas during the previous winter (e.g., Naveira Garabato et al. 2009). PV and oxygen data for the two water masses indicate that both are ventilated in the vicinity of the study region (Fig. 6), with the PV minimum in the SAMW density range and oxygen maximum at the core of the AAIW range suggesting the influence of surface waters. (Oxygen data are sourced only from the dynamic height bin lying closest to the PF. This range is chosen in order to demonstrate the signal most clearly, with the maximum being rapidly eroded by mixing in profiles located farther north.) In the following section, the locations of these formation areas for SAMW and AAIW are identified and the key mechanisms responsible for forcing the surface properties in these regions are determined. It is anticipated that these surface changes, forced during winter, are later manifest in the water masses measured in Drake Passage in summer. This relationship between the mixed layer and subducted water mass properties will be considered in the discussion at the end of the section.

Maps of the correlation between mean (spring–summer) mode and intermediate water potential temperature (during 1993–2009, a period in which the property time series is densely populated and its quality well quantified) and the mean SST from the previous winter (defined as July–September) are shown in Fig. 7. Spatially coherent areas of significant correlation are evident for both water masses, suggesting their ventilation in these regions during the winter. A band of significant influence for SAMW may be identified straddling Drake Passage, centered at ~58°S, and extending from 65° to 110°W. For AAIW, areas of significant correlation are found both to the north and south of the passage, lying adjacent to the Chilean coast north of 55°S and in the northern Bellingshausen Sea at ~65°S in the south. This pattern suggests some degree of coherent modulation of the properties to the north and south of the passage. A lagged correlation analysis of SST (not shown) indicates that, as discussed by Meredith et al. (2008), surface water properties may be modified further west in the central South Pacific (e.g., via ENSO-related atmospheric teleconnections) and then advected eastward toward Drake Passage. In such an analysis, a split in the modified area may be traced, with part of the modified mass being advected eastward and then northward along the coast of South America and part being advected into the Bellingshausen Sea. This split, as well as the ensuing advection, thus leads to two highly correlated areas of surface waters lying to the north and south of Drake

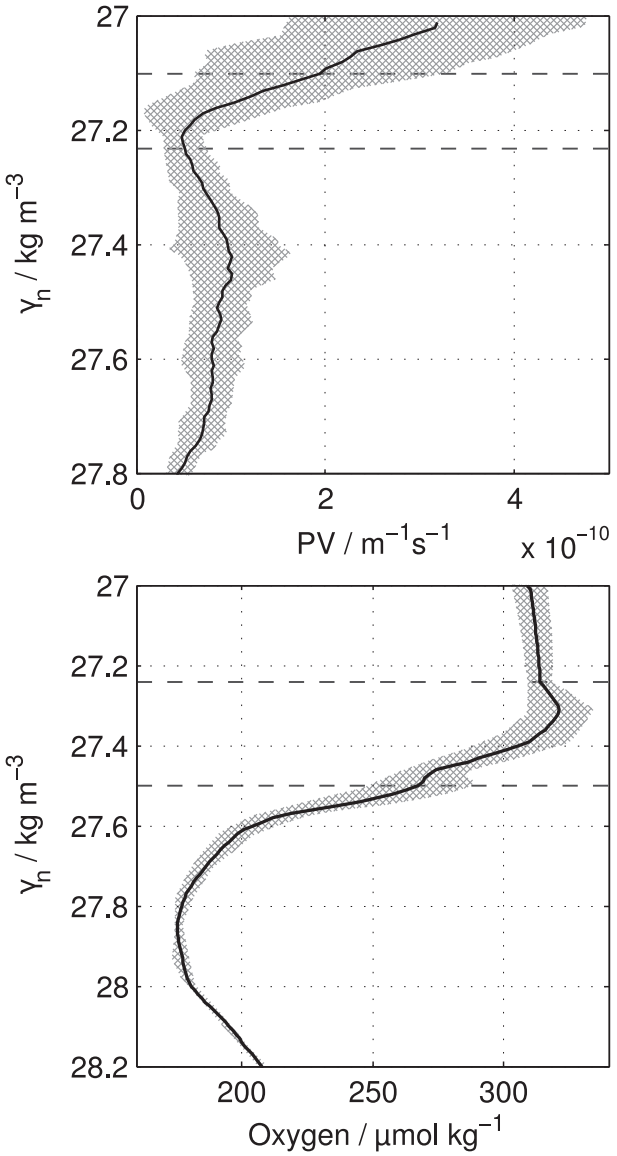

FIG. 6. (top) Mean potential vorticity profile averaging all data lying to the north of the Subantarctic Front. (bottom) Mean oxygen profile, created by averaging all available data (comprising the 1997, 1999, and 2009 sections listed in Table 1) immediately to the north of the PF. For oxygen, the bin width is selected to correspond to that used in the creation of the background fields, and the data are thus sourced from the region $0.54 \leq \phi_{500-1500} \leq 0.57$ dyn m. Data lying in the upper 120 dbar of the water column are excluded from both means. Gray dashed lines denote the water mass boundaries, while hatched areas show the standard deviation envelopes.

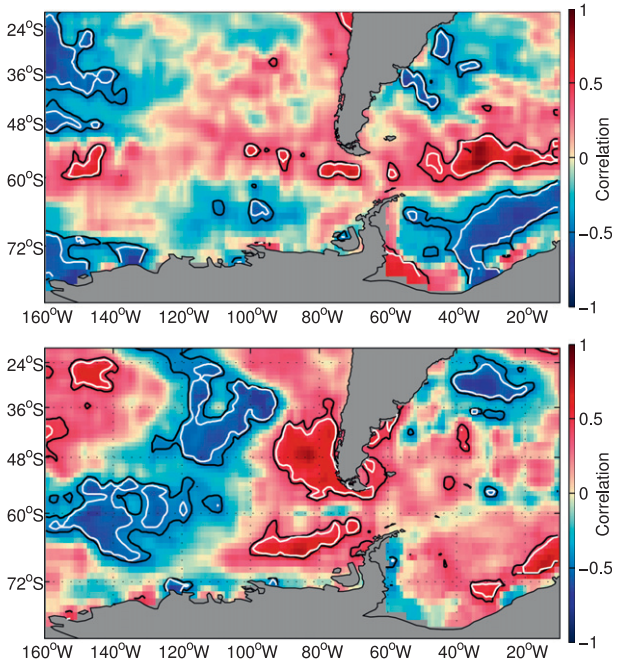

FIG. 7. Correlation between (top) SAMW and (bottom) AAIW summer potential temperature and SST anomaly the previous winter over 1994–2009. Black (white) contours indicate 90% (95%) significance levels.

Passage, as evident in Fig. 7. The two areas may further experience coherent change as a result of large-scale atmospheric forcing associated with the modification of the atmospheric pressure field around the ASL. Additional lagged correlation analysis of SST shows the propagation of the highly correlated area in the Bellingshausen Sea northeastward along the tip of the peninsula and toward the region sampled in our time series analysis. This southern region is thus selected as the control area to investigate the forcing mechanisms of AAIW property variability.

Wind stress may be anticipated to play a significant role in driving interannual variability in SAMW due to the crucial role of intensified overturning in the water mass' formation (McCartney 1977). As with SST, zonal wind stress from the previous winter is correlated with the spring–-summer-mean SAMW temperature and salinity. The analysis was repeated for ERA-Interim and NCEP–NCAR reanalysis (hereafter NCEP) with no significant difference found between the two and, for consistency with previous work in the literature suggesting that the ERA-Interim (hereafter ERA) provides a more accurate representation of high-latitude atmospheric processes than the NCEP product (Bromwich and Fogt 2004; Hines et al. 2000), the results obtained with the ERA are shown in the figures presented here.

Correlations between SAMW (AAIW) potential temperature and winter-mean zonal wind stress are shown in Fig. 8 (Fig. 9). The bands of strong positive correlation lying adjacent to the South American coast to the north of the passage and strong negative correlation spanning the Bellingshausen Sea in the south highlight the local northward–southward displacement of the circumpolar

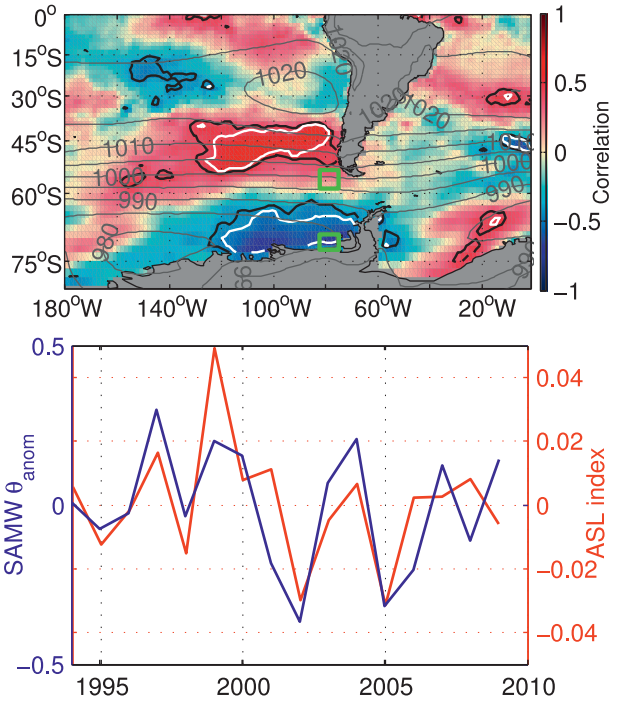

FIG. 8. (top) Correlation between zonal wind stress anomaly and SAMW θ anomaly over 1994–2009. Black (white) contours indicate 90% (95%) significance levels. Gray contours denote the mean wintertime atmospheric pressure. Green boxes indicate the areas used in the calculation of the ASL index. (bottom) Time series of detrended SAMW potential temperature anomaly (blue) and ASL index (red).

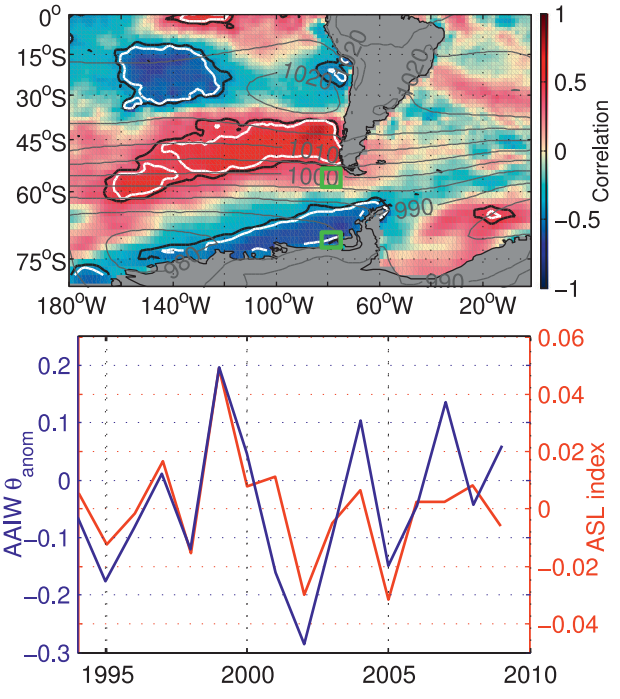

FIG. 9. As in Fig. 8, but for AAIW.

zonal westerlies in this area, associated with changes in curvature and/or intensity of the ASL. These patterns are evident in both figures, suggesting that a coherent mode of atmospheric forcing influences both water masses on interannual time scales. The wider pattern of alternating negative and positive correlations extending southeastward from the tropical western South Pacific and culminating in a positive anomaly in the Weddell Sea is further suggestive of the PSA teleconnection associated with ENSO, which in turn may act to modify the ASL, as discussed above.

To enable comparison of the large-scale forcing with water mass properties on interannual and longer time scales, it is useful to characterize the behavior of the ASL with a simple index. Two areas lying near the eastern perimeter of the ASL (and indicated by green boxes in Figs. 8, 9) are selected as the basis for this index, given their locations in the northern and southern limbs of the climatological ASL and their geographical proximity to Drake Passage. The two areas are noted to experience substantial changes in wind stress curl as the intensity and the eastern-perimeter geometry of the ASL vary on interannual time scales (this impact is demonstrated further in Fig. 15). The difference between the wind stress curl values in the two regions yields an index that increases either when the low deepens or the curvature of the low's eastern edge is accentuated. This index is significantly correlated with both the maximum depth of the low ($r = -0.46$) and its latitude ($r = 0.52$), thus describing both the intensity of the ASL and changes in its relative geometry. The bottom panel of Fig. 8 (Fig. 9) compares time series of the ASL index defined above with the record of SAMW (AAIW) temperature anomaly. The ASL index and both the SAMW and AAIW θ anomaly time series are significantly correlated at the 95% level, with $r = 0.65$ for SAMW and $r = 0.73$ for AAIW. A similar significant relationship is identified between the neutral density at the SAMW core and the ASL's wind stress footprint (Fig. 10: $r = -0.65$). However, the relationship between neutral density at the AAIW core and the ASL is a little more complex (Fig. 11): AAIW neutral density correlates significantly with the wintertime sea ice concentration anomaly west of the Antarctic Peninsula, which is in turn influenced by the intensity of meridional winds west of the peninsula associated with the ASL (Fig. 11b; see also Harangozo 2006). This points to a mechanistic link between AAIW neutral density and the ASL, although no statistically significant relationship between the two parameters can be directly identified in the available data record. The associations between the

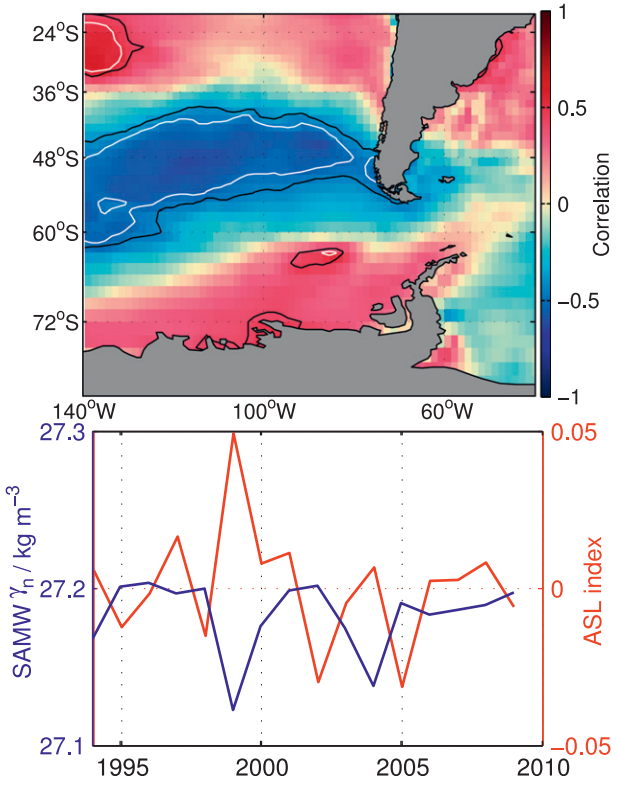

FIG. 10. (top) Correlation between spring–summer SAMW neutral density at salinity maximum and winter zonal wind stress over 1993–2009. Black (white) contours indicate 90% (95%) significance levels. (bottom) Time series of SAMW neutral density at salinity maximum and ASL index the previous winter.

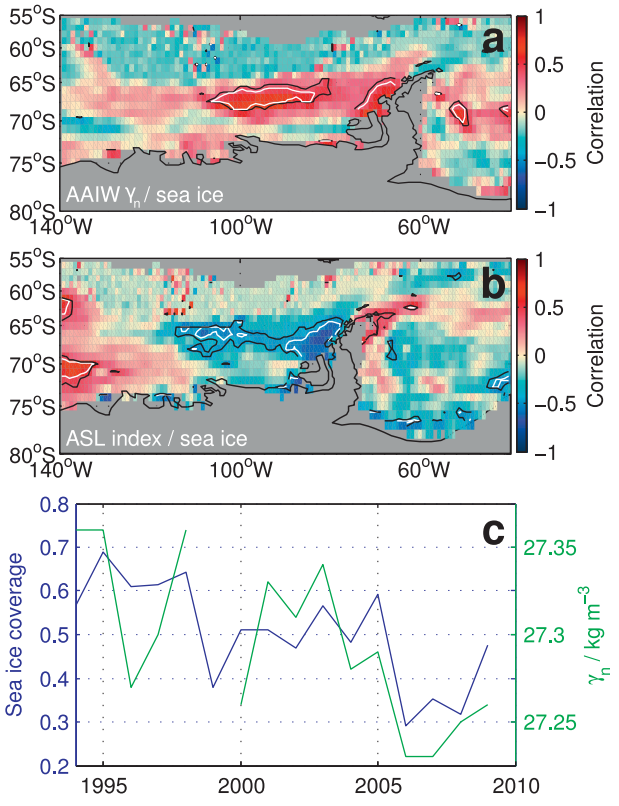

FIG. 11. As in Fig. 10 (top), but for the AAIW neutral density at salinity minimum and sea ice concentration over 1993–2009. (b) Correlation between sea ice concentration and ASL index. (c) Time series of winter sea ice concentration in the control area and AAIW neutral density the following summer.

mode and intermediate water densities and the ASL index unveiled here are in the sense of an anomalously strong (weak) ASL inducing a decrease (an increase) in density in both water masses. Having established the existence of a robust relationship between the intensity of the ASL and the hydrographic properties of mode and intermediate waters in the Drake Passage region, the physical mechanisms underpinning that relationship are investigated next.

a. SAMW

SAMW salinity variability on the time scales of concern to this study may be induced by two main mechanisms: the northward Ekman transport of Antarctic surface waters and/or the freshwater flux across the ocean surface. Temperature variability may also be driven by the Ekman transport, with the air–sea turbulent heat flux being another potential contributor. The possible contributions to the observed SAMW variability made by these mechanisms are evaluated below within the SAMW formation area (defined using the area of significant correlation highlighted in Fig. 7 to span the region 57°–60°S, 65°–80°W).

Changes in the northward Ekman transport of freshwater into the region of SAMW formation may be estimated, following Rintoul and England (2002), using

$$S_{\text{anom}} = \frac{\tau_{x(\text{anom})}\Delta t(S_f - S_{\text{EK}})}{\rho_0 f L_y H},$$

where S_{anom} is the SAMW salinity anomaly that results from an observed zonal wind stress anomaly $\tau_{x(\text{anom})}$, ρ_0 is the density of seawater ($\sim$1027 kg m^{-3}), f is the inertial frequency ($\sim 1.2 \times 10^{-4}$ s^{-1}), L_y is the meridional extent of the SAMW formation region ($\sim$350 km, estimated from the 95% significance bounds in Fig. 7 to span $\sim$3° of latitude), H is the depth of the winter mixed layer ($\sim$400 ± 120 m, estimated using a potential density criterion of $\Delta\sigma_\theta = 0.03\sigma_0$ applied to winter in situ data), S_f is the characteristic SAMW salinity after modification (34.17 ± 0.04, the mean value in the control area estimated from in situ springtime data), S_{EK} is the salinity of the Antarctic surface waters flowing northward in the Ekman layer (33.86 ± 0.06, the mean value at the

southern edge of the control area in winter), and Δt is the length of the winter season (3 months). Similarly, the equivalent expression for potential temperature is

$$\theta_{\text{anom}} = \frac{\tau_{x(\text{anom})}\Delta t(\theta_f - \theta_{\text{EK}})}{\rho_0 f L_y H},$$

where θ_f is the potential temperature of SAMW after modification (4.5° ± 0.4°C, the mean value in the control area estimated from in situ summer data), θ_{EK} is the potential temperature of the water flowing north in the Ekman layer (2.5° ± 0.6°C, the mean value at the southern edge of the control area, again from wintertime in situ data), and θ_{anom} is the potential temperature anomaly resulting from an observed zonal wind stress anomaly $\tau_{x(\text{anom})}$.

The contribution of changes in net wintertime precipitation to the observed variability in SAMW salinity may be assessed using the salinity conservation equation,

$$\Delta S = \frac{F_{\text{anom}} S_f \Delta t}{H},$$

where ΔS is the change in SAMW salinity brought about by a change of F_{anom} in the freshwater flux through the ocean surface. The net precipitation anomaly may be obtained from the atmospheric reanalysis fields by combination of evaporation and precipitation rates. In assessing the contribution of precipitation to the observed salinity changes, H is estimated to be ~175 m, reflecting the abrupt reduction in mixed layer depth (MLD) in the central Drake Passage relative to the deeper values occurring in the adjacent southeast Pacific (de Boyer Montégut et al. 2004) and thus leading to a greater effect on salinity here. The control area for E–P thus lies in the central Drake Passage, with correlation maps (not shown) supporting the hypothesis that the primary area of influence lies slightly downstream of the primary formation area previously identified in Fig. 7.

The magnitude of temperature variability that can be plausibly induced by air–sea turbulent heat fluxes may be calculated using

$$\theta_{\text{anom}} = \frac{Q_{\text{anom}}\Delta t}{\rho_0 c_p H},$$

where θ_{anom} is the potential temperature change in SAMW resulting from an observed air–sea turbulent heat flux anomaly Q_{anom} and c_p is the specific heat capacity of seawater (~3986 J kg^{-1} K^{-1}). It is possible to calculate the air–sea turbulent heat flux directly from the reanalysis fields by combining sensible and latent heat fluxes, leading to a direct estimate of Q. Removal of the mean annual cycle over the period examined here (1993–2008) then yields Q_{anom}.

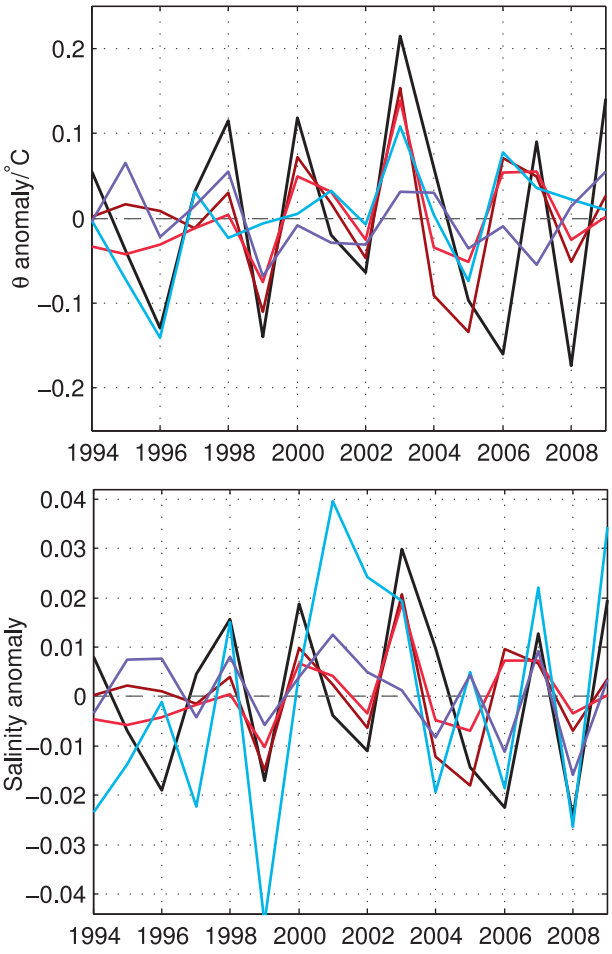

FIG. 12. Time series of estimated contributions by Ekman transports, air–sea turbulent heat flux, and evaporation–precipitation balance to changes in SAMW (top) θ and (bottom) salinity. The solid black line shows the observed detrended water mass property variability; the light (dark) red line shows the ERA (NCEP) Ekman transport term; and the blue (purple) line indicates the ERA (NCEP) air–sea turbulent heat flux contribution (for θ) and the net precipitation contribution (for salinity).

By substituting the wintertime $\tau_{x(\text{anom})}$, F_{anom}, and Q_{anom} in the SAMW control region from the reanalysis products into the above equations, estimates of the contributions of the various mechanisms to the induction of SAMW thermohaline anomalies are obtained. The results of this are shown in Fig. 12 and summarized in Table 3, along with associated uncertainties.

The variability observed in SAMW is best explained by a combination of mechanisms, both in temperature and salinity. In temperature, the Ekman contribution appears to be of somewhat larger amplitude and better correlated with the observed properties than that of the

TABLE 3. Contributions of different mechanisms to observed interannual variability in SAMW properties. Correlations are between estimated properties (from calculations described in section 4) and observed SAMW anomalies on pressure surfaces. Errors are estimated from the standard deviation of estimated in situ MLD, salinity, and temperature properties as detailed in section 4. The magnitude of the estimates suggests that interannual changes in potential temperature are induced by a combination of air–sea turbulent heat fluxes Q_{anom} and Ekman heat transports, while salinity changes are controlled by a combination of the *E–P* balance and Ekman transport. All variables are detrended.

Temperature			
Mechanism	*r*	Mean variability (°C)	Error (°C)
Observed		0.17	
NCEP Q_{anom}	0.44	0.05	0.02
ERA Q_{anom}	0.37	0.07	0.03
NCEP Ekman	0.56	0.10	0.02
ERA Ekman	0.57	0.06	0.02

Salinity			
Mechanism	*r*	Mean variability	Error
Observed		0.025	
NCEP *E–P*	0.57	0.012	0.011
ERA *E–P*	0.68	0.032	0.012
NCEP Ekman	0.54	0.013	0.003
ERA Ekman	0.56	0.008	0.003

air–sea turbulent heat flux. In salinity, the derived *E–P* contribution is a little larger and better correlated than that of the Ekman transport. However, the differences in contribution of the various mechanisms are not sufficiently distinct to suggest that one robustly dominates the other, either in temperature or salinity. We thus conclude that the northward Ekman transport of Antarctic surface waters, the *E–P* balance, and air–sea turbulent heat fluxes all contribute significantly to SAMW thermohaline variability on interannual time scales.

b. AAIW

In addition to the mechanisms outlined in the previous subsection, the surface water properties in the Bellingshausen Sea control area (defined using the southern area highlighted in the correlation analysis of Fig. 7, as discussed above), from which AAIW is ventilated, may also be influenced by the annual brine/freshwater cycle associated with sea ice formation and melting. Following Watanabe et al. (2004), the heat conservation equation

$$\rho_i hL + \rho_i hC(\theta - \theta_f) = \rho_0 HC(\theta_w - \theta)$$

may be rearranged to yield

$$\Delta\theta = \frac{\rho_i h}{\rho_0 H}\left(\theta_f - \theta_w - \frac{L}{c_p}\right),$$

where θ is the temperature after the addition of the meltwater admixture and $\Delta\theta$ is the change in water temperature resulting from the sea ice melt, ρ_i is the density of ice ($\sim$930 kg m^{-3}), ρ_0 is the density of seawater in the mixed layer ($\sim$1027 kg m^{-3}), h is the area-averaged sea ice thickness anomaly, H is the mixed layer depth (estimated using winter–spring data to be approximately 150 $\pm$ 25 m, again using the same density criterion as for SAMW), θ_f is the freezing temperature of seawater (-1.8°C), θ_w is the potential temperature of the water in the mixed layer before the addition of the meltwater admixture ($-0.8° \pm 0.5$°C), L is the latent heat of freezing ($\sim 2.93 \times 10^5$ J kg^{-1}), and c_p is the specific heat capacity of seawater ($\sim$3986 J kg^{-1} K^{-1}). As in Naveira Garabato et al. (2009), the crude (yet presently unavoidable) assumption of a simple proportionality between sea ice concentration and sea ice production is adopted. The sea ice thickness anomaly is thus estimated using $h \sim (h_t d_{\text{anom}} E)/L_y$, where h_t is the characteristic sea ice thickness in the control area [estimated from Timmermann et al. (2004) to be approximately 0.5–1 m], d_{anom} is the anomaly in winter sea ice extent (obtained from satellite measurements of sea ice concentration), $E \sim 0.7$ defines a characteristic late-winter sea ice concentration of the ice-covered sector of the control area, and L_y is the meridional extent of the control area (approximately 500 km). These values lead to a range of plausible wintertime sea ice thickness anomalies of approximately 5–20 cm in the control area.

Again, following Watanabe et al. (2004), the salinity change in the surface water of the Bellingshausen Sea control area due to the addition of meltwater may be estimated as

$$\Delta S = \frac{\rho_i h S_i - \rho_0 h S_w}{\rho_0 H}.$$

The salinity of sea ice, S_i, is approximately 5 (Gough et al. 2012) and the salinity of the Winter Water before mixing S_w, 33.90 $\pm$ 0.09 (estimated from in situ spring data), with other values in the equation as defined above. The meridional extent anomaly, derived from satellite data, is substituted into the above equation, yielding an estimate of salinity variability due to sea ice melt. The contributions of Ekman flows, the air–sea turbulent heat flux and changes in the evaporation–precipitation balance are estimated as for SAMW. All gradients are defined across the AAIW control area, thus yielding values of $L_y = 500$ km, $f = -1.3 \times 10^{-4}$ s^{-1}, $H = 150 \pm 25$ m, $S_f = 33.80 \pm 0.09$, $S_{\text{EK}} = 34.10 \pm 0.05$, $\theta_f = -0.2° \pm 0.6$°C, and $\theta_{\text{EK}} = -1.7° \pm 0.04$°C. The resulting contributions from the various mechanisms are

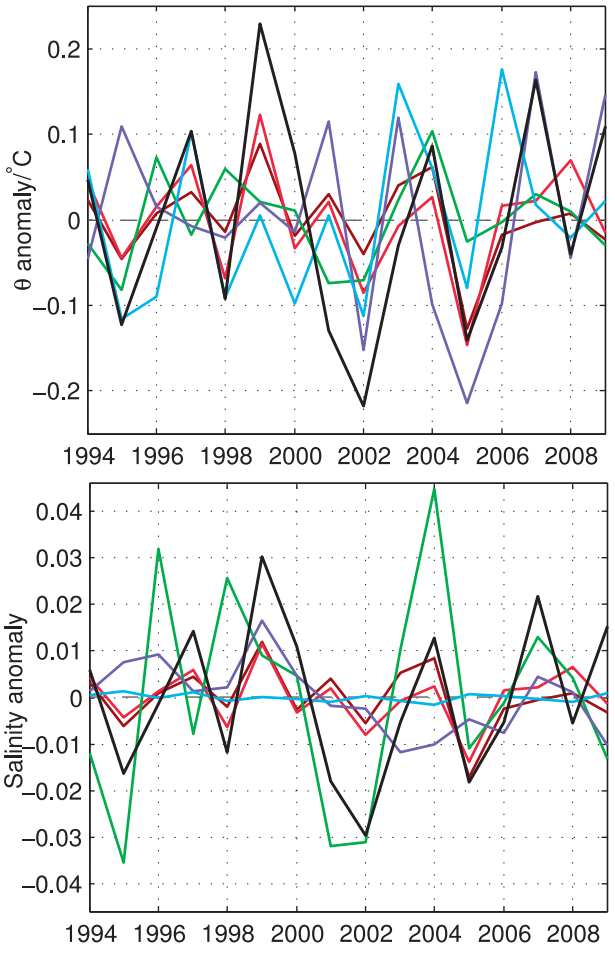

FIG. 13. As in Fig.12, but for AAIW and including sea ice formation with the green line denoting the sea ice formation contribution.

shown in Fig. 13 and synthesized in Table 4 with error estimates.

The mechanism accounting for the greatest fraction of the observed AAIW potential temperature variability is the air–sea turbulent heat flux, with the Ekman term and winter sea ice formation both appearing to play a smaller, although nonnegligible, role (Table 4). In contrast, salinity variability is predominantly controlled by the influence of springtime freshwater input due to sea ice melt, with the Ekman and evaporation–precipitation contributions being of substantially smaller magnitude and, in the case of the evaporation–precipitation balance, less correlated with the observed AAIW salinity changes. The correlation with the air–sea turbulent heat flux is visibly increased in the second half of the time series relative to the first, coincident with an accelerated retreat of the winter sea ice in the formation area. It is suggested that the two are connected, with the strengthened northerly winds incident on the Bellingshausen Sea,

TABLE 4. Contributions of different mechanisms to observed interannual variability in AAIW properties. Correlations are between estimated properties (from calculations described in section 4) and observed AAIW anomalies on pressure surfaces. Errors are the difference in mean variability between the contributions calculated using the given values and the same calculation using the mean ± standard deviations as detailed in section 4 (where multiple variables have errors the greatest possible difference is given as error). The magnitude of the estimates suggests that interannual changes in potential temperature are induced by air–sea turbulent heat fluxes Q_{anom}, while salinity changes are most plausibly driven by variations in sea ice production.

Temperature			
Mechanism	r	Mean variability (°C)	Error (°C)
Observed		0.17	
NCEP Q_{anom}	0.36	0.14	0.02
ERA Q_{anom}	0.55	0.13	0.01
NCEP Ekman	0.59	0.01	0.08
ERA Ekman	0.68	0.01	0.08
Sea ice	0.57	0.06	0.01

Salinity			
Mechanism	r	Mean variability	Error
Observed		0.023	
NCEP E–P	0.26	0.006	0.001
ERA E–P	−0.06	0.001	0.001
NCEP Ekman	0.58	0.009	0.003
ERA Ekman	0.67	0.010	0.003
Sea ice	0.64	0.027	0.009

regularly associated with an intensified ASL, creating anomalously warm surface conditions and thus limiting sea ice formation. This simultaneously exposes greater areas of the sea surface directly to the intensified winds, facilitating increased air–sea turbulent heat flux and leading to a net warming in the control area. (This sequence of processes is summarized schematically in Fig. 16.)

c. *Discussion*

The observed interannual-scale correlation between SAMW and AAIW properties and the wintertime wind stress field in the southeast Pacific–Drake Passage region, as well as our quantification of the various terms in the SAMW and AAIW heat and freshwater budgets in the preceding subsections, suggest that the regional mode and intermediate water characteristics are largely controlled by the ASL. In the case of SAMW, this control is exerted via the modulation of the winter Ekman transport of cold and fresh Antarctic surface waters across the SAF, air–sea turbulent heat fluxes, and the E–P balance. For AAIW, the ASL regulates the properties of the precursor Winter Water mainly via its influence on wintertime air–sea turbulent heat fluxes and sea ice formation (followed by springtime melting)

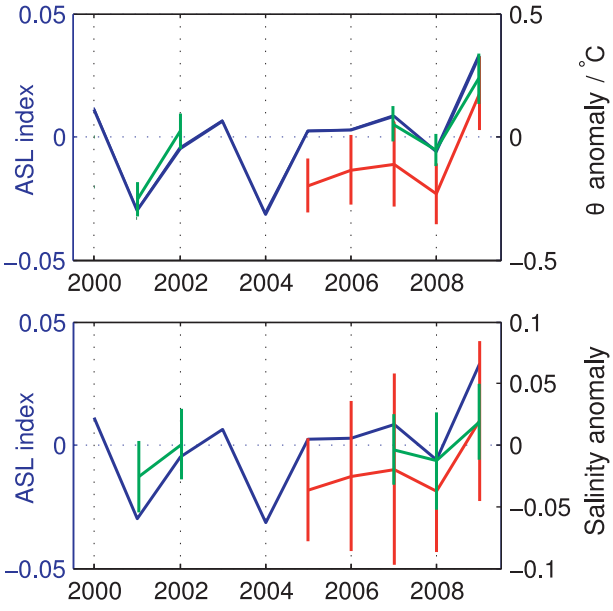

FIG. 14. Time series of winter mixed layer (top) temperature and (bottom) salinity properties in the SAMW (red) and AAIW (green) formation areas (as defined in Fig. 7). The ASL index is shown in blue.

in the Bellingshausen Sea. While winter measurements are still not widely available in the study region, there exist a few years in which observations from this season exist, and the relationship between the properties of the winter mixed layer (defined here to span the upper 120 dbar of the water column) in the water mass formation regions and the ASL index is shown in Fig. 14. Despite the limited data availability, the good correspondence between mixed layer properties and the ASL index adds further support to the scenario of controlling mechanisms outlined above. Further, the patterns of variability correspond well with those observed in the summer SAMW and AAIW properties, again adding credence to the notion that these directly modified winter surface waters supply the water masses observed in summer.

Our results on the mechanisms regulating the SAMW and AAIW heat and freshwater budgets show some consistency with a number of previous related studies. For example, in considering the driving mechanisms of temporal variability in SST across the Southern Ocean, Verdy et al. (2006) and Ciasto and England (2011) both found air–sea turbulent heat fluxes and Ekman transport to contribute comparably, noting a significant role of both ENSO and the SAM in driving that variability. An importance of both Ekman and air–sea turbulent heat flux contributions to the SAMW heat budget was also found by the exploratory analysis of Naveira Garabato et al. (2009) in the Drake Passage region and by Sallée et al. (2006) in their study of SAMW formation in the Southeast Indian Ocean. In contrast, Rintoul and England (2002) suggested an overwhelming dominance of the Ekman heat transport in inducing interannual variability in SAMW properties south of Australia, which [similarly to the SST-focused studies of Verdy et al. (2006) and Ciasto and England (2011)] points to the existence of considerable regional variability in the balance between Ekman and air–sea turbulent heat flux terms. Finally, our finding of AAIW properties being set primarily through ventilation by Winter Water formed in the Bellingshausen Sea is consistent with previous work highlighting the significance of this process in influencing AAIW characteristics in Drake Passage and the wider South Atlantic (Meredith et al. 1999; Naveira Garabato et al. 2009; Saenko and Weaver 2001). This notion is also supported by an analysis of the seasonal cycle of water mass properties in our study domain (not shown; see Close 2011). Whereas SAMW is coolest and freshest in winter (consistent with the paradigm of the water mass being formed by winter convection north of the SAF; McCartney 1977), AAIW is coolest and freshest in spring, which suggests that the process of ventilation across the PF has a characteristic time scale of a few months and that the Winter Water subducting at the front is influenced by cold and fresh sea ice melt admixtures.

The atmospheric circulation associated with anomalous states of the ASL is illustrated by Fig. 15, where the mean sea level pressure field of the four years within the 1979–2009 period for which the ASL index is largest and positive is compared with an analogous composite for the four years in which the ASL index is largest and negative. While individual years can deviate somewhat from this general pattern, the figure suggests that, when the ASL index is positive, the low is deeper and expands northward over the area to the west of the South Pacific high. Nearer Drake Passage, isobars are shifted southward as the curvature around the ASL's eastern edge increases, and the zonal wind stress over northern Drake Passage is reduced (Figs. 15a,b). Concurrently, the meridional flow onto the west Antarctic Peninsula is intensified (Figs. 15a,c). In turn, when the ASL index is negative, the eastward wind stress over the SAMW formation area increases, while the southward wind stress onto the west Antarctic Peninsula is reduced as the ASL adopts a more zonal configuration, expanding over the Bellingshausen Sea.

This behavior of the ASL and the way in which it influences water mass properties in the Drake Passage region is described schematically in Fig. 16. When the ASL is strong, zonal wind stress over the SAMW formation area is weak. SAMW thus becomes relatively

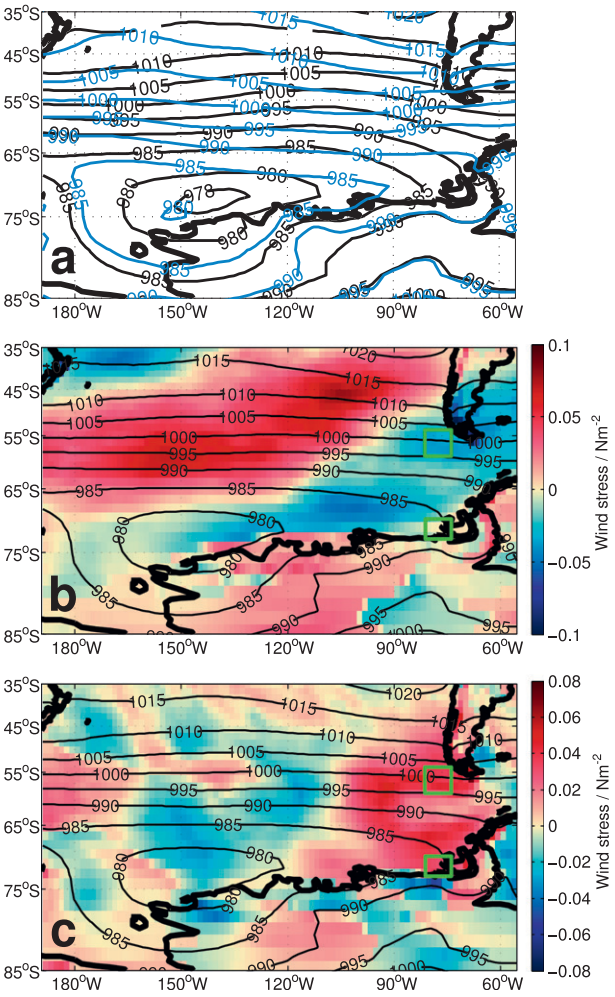

FIG. 15. (a) Composite SLP field for the four highest (black) and four lowest (blue) wintertime ASL index states. (b) Difference in zonal wind stress between the ASL high and low index states (high – low). (c) Difference in meridional wind stress between the ASL high and low index states (high – low). Black contours in (b),(c) show mean wintertime SLP field calculated over the 1979–2009 period, for reference. Green boxes indicate the areas used in the calculation of the ASL index.

warm, saline, and light as the wintertime northward Ekman transport of Antarctic surface waters, net precipitation, and air–sea turbulent heat fluxes are reduced. Similarly, when the ASL is strong, meridional wind stress onto the west Antarctic Peninsula (WAP) intensifies, leading to reduced sea ice extent and increasing air–sea turbulent heat fluxes. AAIW warms because of increased anomalously warm northerly air being advected over the Bellingshausen Sea and salinifies because of reduced sea ice melt in the spring, leading to a decrease in density. The reverse scenario occurs during weak ASL events, with strong zonal wind stress over the SAMW formation area driving the production of cool, fresh, and dense modes of the water mass, while the weakened meridional wind stress onto the WAP leads to increased sea ice extent; decreased air–sea turbulent heat fluxes; and the production of anomalously cool, fresh, and dense AAIW.

The evolution of the wintertime ASL over the period of this study is shown in Fig. 17. The ASL weakens slightly between the winter averages of 1994–99 and 2000–04, before reaching a deeper mean state during the 2005–09 pentad. There is also a suggestion of a change in the geometry of the ASL within the 1990–2009 period, with an analysis of the location of the deepest point of the low suggesting a general northeastwards migration, starting in approximately 2005. The ASL index shows a decreasing trend over 1979–2005, in contrast to the sharp increase in the index over 2005–10 (resulting in a net increasing trend over 1979–2010). This evolution is consistent with the observed water mass variability in Drake Passage, in the light of the mechanisms of water mass modification inferred in the previous discussion. Between 1994 and 2005, SAMW is relatively cool, consistent with the weaker state of the ASL, and warms slightly after 2005 as the low intensifies (the salinity behavior is more difficult to attribute here, possibly because of other influences on interdecadal time scales). Similarly, AAIW is comparatively cold and fresh over 1990–2005, as the weaker state of the ASL permits greater sea ice coverage, reducing air–sea turbulent heat flux and supplying fresh meltwater in spring. After 2005, the ASL becomes increasingly positive, leading to the observed warming and salinification of AAIW over 2005–09.

5. Conclusions

The properties of SAMW and AAIW in Drake Passage have been shown to have undergone substantial changes over recent decades. The interdecadal freshening tendency that has dominated SAMW variability in this region over the past three decades has recently abated, while AAIW has undergone a significant warming since the earlier analysis of Naveira Garabato et al. (2009). These trends in salinity and temperature are accompanied by strong tendencies in pressure in the region (not believed to be linked to the processes discussed here). The interannual-to-interdecadal temperature and salinity variability is accompanied by changes in density, with both SAMW and AAIW observed to have experienced a substantial lightening since the 1970s.

The recent availability of year-round in situ data through the Argo program and associated initiatives has been shown to permit identification of the processes forcing water mass variability on interannual time scales.

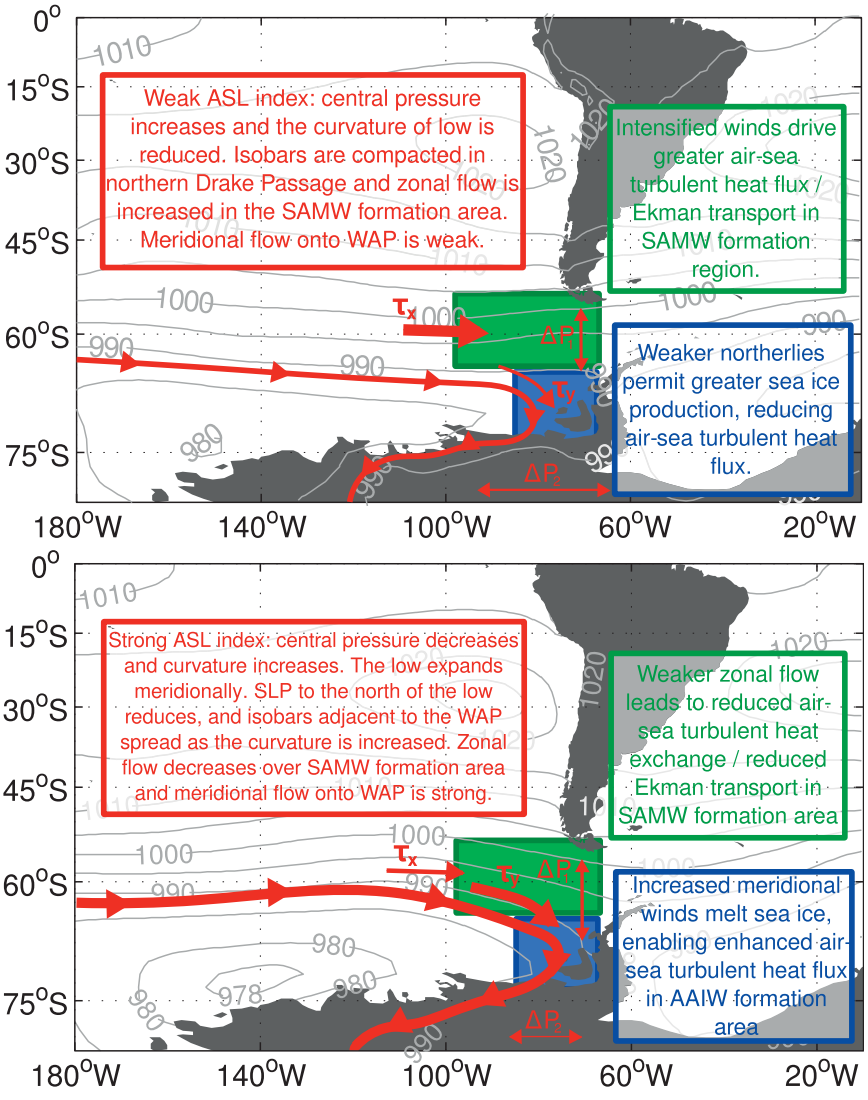

FIG. 16. Schematic representation of the control exerted by the ASL on SAMW and AAIW characteristics in the Drake Passage region, during a (top) weak and (bottom) strong ASL state. Gray isobars in the weak (strong) ASL schematic show mean SLP of the four years in which the index is most negative (positive) over 1979–2010. The term ΔP_1 indicates the meridional distance between the 1000- and 990-hPa isobars (i.e., a metric of the zonal wind stress in northern Drake Passage) and ΔP_2 denotes the zonal distance between the 985- and 990-hPa isobars at the WAP (i.e., a metric of meridional wind stress onto the Bellingshausen Sea).

The significant relationships identified between the observed interannual variability in water mass properties and the estimated contributions to those changes from different air–sea ice interaction mechanisms suggest a significant role of the ASL in regulating water mass properties in the Drake Passage region on interannual and interdecadal time scales. SAMW and AAIW are found to be influenced at first order by distinct mechanisms, with variations in SAMW temperature characteristics being driven primarily by Ekman fluxes (with air–sea turbulent heat fluxes also exerting a significant influence), while the salinity properties are set by a combination of Ekman transport and variability in the *E–P* balance. Changes in AAIW properties have been most strongly shaped by wintertime air–sea turbulent heat fluxes and springtime sea ice melting in the Bellingshausen Sea. Thus, on interannual time scales, the properties of the two water masses are set by different mechanisms but ultimately driven by the same large-scale atmospheric forcing.

Changes in the ASL have been extensively highlighted as the most prominent expression of nonannular

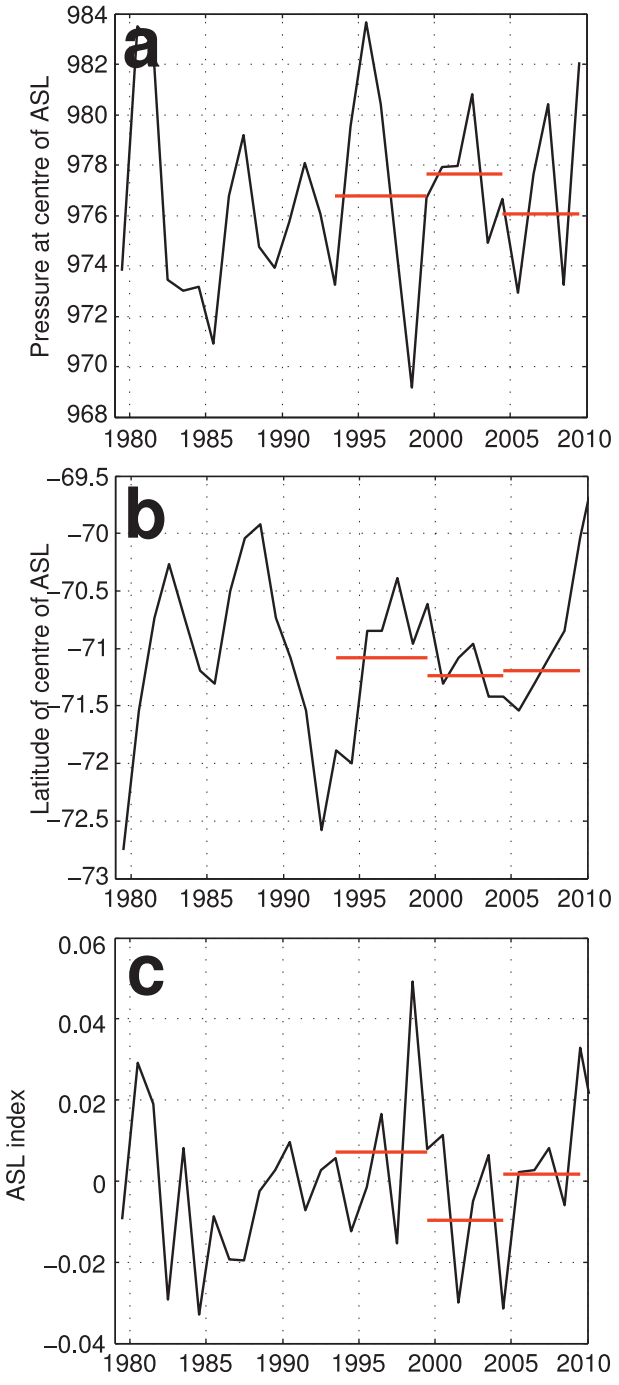

FIG. 17. Evolution of (a) minimum pressure in the ASL, (b) latitude of that minimum pressure, and (c) ASL index, defined to reflect the variability of the two measures over time (see section 4). The red lines indicate pentadal wintertime averages corresponding to the year groups defined in Fig. 4.

variability in the Antarctic and Southern Ocean climate system and linked to the major modes of Southern Hemisphere climate variability. For example, Lefebvre et al. (2004) showed that the SAM has a pronounced nonannular component that generates low (high) pressure anomalies to the west of the Antarctic Peninsula during strongly positive (negative) SAM events, thereby mapping onto the ASL. Similarly, several authors (e.g., Carleton 2003; Yuan and Li 2008) demonstrated that tropical Pacific forcing associated with ENSO is rapidly transmitted to the southeast Pacific via the PSA standing wave train and modulates the intensity and geometry of the ASL. Fogt et al. (2011) emphasized the role of the interaction between the SAM and ENSO in shaping the response of the ASL to large-scale climate variability. Given the attribution of the recent interdecadal intensification of the (summer) SAM and the (autumn) ASL to stratospheric ozone loss (Marshall 2003; Thompson and Solomon 2002; Turner et al. 2009), the ASL-mediated evolution of mode and intermediate water mass properties discussed here may already include an anthropogenic footprint. The prediction of a further strengthening of the (particularly winter) SAM over the twenty-first century (Thompson et al. 2011) associated with greenhouse gas forcing heralds further decadal-scale changes in the water masses entering the South Atlantic through Drake Passage and calls for a continuation of monitoring activities in the region.

Acknowledgments. This study would not have been possible without the effort of many people at sea and ashore to collect, calibrate, and process the Drake Passage section measurements. The U.K. Natural Environment Research Council (NERC) funded 17 of the section occupations used in this work through Research Grant GR3/11654 and several core-strategic research programs at the National Oceanography Centre, Southampton (NOCS) and the British Antarctic Survey. It also funded the SEaOS project through Research Grant NER/D/S/2002/00426 and supported SEC through a Ph.D. studentship based at NOCS and ACNG through an NERC Advanced Research Fellowship (NE/C517633/1). Argo profile data were made available by the International Argo Project. We are grateful to Eleanor Frajka-Williams and Mike Meredith for helpful discussions and to two anonymous reviewers for their constructive comments on the manuscript.

REFERENCES

Aoki, S., M. Harimaya, H. Mitsudera, H. Sasaki, and Y. Sasai, 2007: Formation regions of Subantarctic Mode Water detected by OFES and Argo profiling floats. *Geophys. Res. Lett.,* **34,** L10606, doi:10.1029/2007GL029828.

Bacon, S., 2002: RRS *James Clark Ross* cruise 67, 19 Nov–17 Dec 2001. Drake Passage repeat hydrography: WOCE southern repeat section 1b—Burdwood Bank to Elephant Island. Southampton Oceanography Centre Cruise Rep. 38, 118 pp.

——, 2003: RRS *James Clark Ross* cruise 81, 18 Dec 2002–02 Jan 2003. Drake Passage repeat hydrography: WOCE southern repeat section 1b—Elephant Island to Burdwood Bank. Southampton Oceanography Centre Cruise Rep. 43, 86 pp.

——, and S. Cunningham, 2005: Drake Passage summary report: Cruises on RRS ''*James Clark Ross*,'' 1993–2000. Drake Passage repeat hydrography: WOCE southern repeat section 1b—Elephant Island to Burdwood Bank. Southampton Oceanography Centre Cruise Rep. 44, 151 pp.

Baines, P. G., and K. Fraedrich, 1989: Topographic effects on the mean tropospheric flow patterns around Antarctica. *J. Atmos. Sci.,* **46,** 3401–3415.

Bindoff, N. L., and J. A. Church, 1992: Warming of the water column in the southwest Pacific Ocean. *Nature,* **357,** 59–62, doi:10.1038/357059a0.

——, and T. J. McDougall, 2000: Decadal changes along an Indian Ocean section at 32°S and their interpretation. *J. Phys. Oceanogr.,* **30,** 1207–1222.

——, and Coauthors, 2007: Observations: Oceanic climate change and sea level. *Climate Change 2007: The Physical Science Basis,* S. Solomon et al., Eds., Cambridge University Press, 385–432.

Biuw, M., and Coauthors, 2007: Variations in behavior and condition of a Southern Ocean top predator in relation to in situ oceanographic conditions. *Proc. Natl. Acad. Sci. USA,* **104,** 13 705–13 710, doi:10.1073/pnas.0701121104.

Boehme, L., M. P. Meredith, S. E. Thorpe, M. Biuw, and M. Fedak, 2008a: Antarctic Circumpolar Current frontal system in the South Atlantic: Monitoring using merged Argo and animal-borne sensor data. *J. Geophys. Res.,* **113,** C09012, doi:10.1029/2007JC004647.

——, S. Thorpe, M. Biuw, M. Fedak, and M. Meredith, 2008b: Monitoring Drake Passage with elephant seals: Frontal structures and snapshots of transport. *Limnol. Oceanogr.,* **53,** 2350–2360, doi:10.4319/lo.2008.53.5_part_2.2350.

——, P. Lovell, M. Biuw, F. Roquet, J. Nicholson, S. E. Thorpe, M. P. Meredith, and M. Fedak, 2009: Technical note: Animal-borne CTD-satellite relay data loggers for real-time oceanographic data collection. *Ocean Sci.,* **5,** 685–695.

Böning, C. W., A. Dispert, M. Visbeck, S. R. Rintoul, and F. U. Schwarzkopf, 2008: The response of the Antarctic Circumpolar Current to recent climate change. *Nat. Geosci.,* **1,** 864–869, doi:10.1038/ngeo362.

Boyer, T. P., and Coauthors, 2009: *World Ocean Database 2009.* NOAA Atlas NESDIS 66, 217 pp.

Bromwich, D. H., and R. L. Fogt, 2004: Strong trends in the skill of the ERA-40 and NCEP–NCAR reanalyses in the high and midlatitudes of the Southern Hemisphere, 1958–2001. *J. Climate,* **17,** 4603–4619.

Bryden, H., E. McDonagh, and B. King, 2003: Changes in ocean water mass properties: Oscillations or trends? *Science,* **300,** 2086–2088, doi:10.1126/science.1083980.

Carleton, A. M., 2003: Atmospheric teleconnections involving the Southern Ocean. *J. Geophys. Res.,* **108,** 8080, doi:10.1029/2000JC000379.

Carval, T., and Coauthors, 2008: User's manual: Version 2.1. Argo Data Management Tech. Rep. ar-um-02-01, 61 pp. [Available online at http://w3.jcommops.org/FTPRoot/Argo/Doc/argo-dm-user-manual.pdf.]

Cavalieri, D., C. Parkinson, P. Gloersen, and H. J. Zwally, cited 2008: Sea ice concentrations from Nimbus-7 SMMR and DMSP SSM/I passive microwave data [1978–2007]. National Snow and Ice Data Center. [Available online at http://nsidc.org/data/nsidc-0051.html.]

Charrassin, J.-B., and Coauthors, 2008: Southern Ocean frontal structure and sea-ice formation rates revealed by elephant seals. *Proc. Natl. Acad. Sci. USA,* **105,** 11 634–11 639, doi:10.1073/pnas.0800790105.

Chen, B., S. R. Smith, and D. H. Bromwich, 1996: Evolution of the tropospheric split jet over the South Pacific Ocean during the 1986–89 ENSO cycle. *Mon. Wea. Rev.,* **124,** 1711–1731.

Church, J. A., J. S. Godfrey, D. R. Jackett, and T. J. McDougall, 1991: A model of sea level rise caused by ocean thermal expansion. *J. Climate,* **4,** 438–456.

Ciasto, L. M., and M. H. England, 2011: Observed ENSO teleconnections to Southern Ocean SST anomalies diagnosed from a surface mixed layer heat budget. *Geophys. Res. Lett.,* **38,** L09701, doi:10.1029/2011GL046895.

Close, S. E., 2011: Southern Ocean water mass variability and its causes. Ph.D. thesis, University of Southampton, 244 pp.

——, and A. C. Naveira Garabato, 2012: Baroclinic adjustment in Drake Passage driven by tropical Pacific forcing. *Geophys. Res. Lett.,* **39,** L19610, doi:10.1029/2012GL053402.

Cunningham, S., 2001: RRS *James Clark Ross* cruise JR55, 21 Nov-14 Dec 2000. Drake Passage repeat hydrography: WOCE southern section 1b—Burdwood Bank to Elephant Island. Southampton Oceanography Centre Cruise Rep. 35, 75 pp.

Curry, R., B. Dickson, and I. Yashayaev, 2003: A change in the freshwater balance of the Atlantic Ocean over the past four decades. *Nature,* **426,** 826–829, doi:10.1038/nature02206.

de Boyer Montégut, C., G. Madec, A. S. Fischer, A. Lazar, and D. Iudicone, 2004: Mixed layer depth over the global ocean: An examination of profile data and a profile-based climatology. *J. Geophys. Res.,* **109,** C12003, doi:10.1029/2004JC002378.

Dee, D. P., and Coauthors, 2011: The ERA-Interim reanalysis: Configuration and performance of the data assimilation system. *Quart. J. Roy. Meteor. Soc.,* **137,** 553–597, doi:10.1002/qj.828.

Durack, P. J., and S. E. Wijffels, 2010: Fifty-year trends in global ocean salinities and their relationship to broad-scale warming. *J. Climate,* **23,** 4342–4362.

——, ——, and R. J. Matear, 2012: Ocean salinities reveal strong global water cycle intensification during 1950 to 2000. *Science,* **336,** 455–458, doi:10.1126/science.1212222.

Fogt, R. L., D. H. Bromwich, and K. M. Hines, 2011: Understanding the SAM influence on the South Pacific ENSO teleconnection. *Climate Dyn.,* **36,** 1555–1576, doi:10.1007/s00382-010-0905-0.

Ganachaud, A., and C. Wunsch, 2000: Improved estimates of global ocean circulation, heat transport and mixing from hydrographic data. *Nature,* **408,** 453–457, doi:10.1038/35044048.

Gille, S. T., 2002: Warming of the Southern Ocean since the 1950s. *Science,* **295,** 1275–1277, doi:10.1126/science.1065863.

——, 2008: Decadal-scale temperature trends in the Southern Hemisphere ocean. *J. Climate,* **21,** 4749–4765.

Gough, A. J., A. R. Mahoney, P. J. Langhorne, M. J. M. Williams, and T. G. Haskell, 2012: Sea ice salinity and structure: A winter time series of salinity and its distribution. *J. Geophys. Res.,* **117,** C03008, doi:10.1029/2011JC007527.

Hanawa, K., and L. Talley, 2001: Mode waters. *Ocean Circulation and Climate: Observing and Modelling the Global Ocean,* G. Siedler and J. Church, Eds., Academic Press, 373–386.

Harangozo, S. A., 2006: Atmospheric circulation impacts on winter maximum sea ice extent in the west Antarctic Peninsula region

(1979–2001). *Geophys. Res. Lett.,* **33,** L02502, doi:10.1029/2005GL024978.

Hawker, E., B. King, and M. Sparrow, 2005: RRS *James Clark Ross* cruise 94, 01 Dec–15 Dec 2003. Drake Passage repeat hydrography: WOCE southern repeat section 1b—Burdwood Bank to Elephant Island. Southampton Oceanography Centre Cruise Rep. 55, 56 pp.

Herraiz-Borreguero, L., and S. R. Rintoul, 2010: Subantarctic Mode Water variability influenced by mesoscale eddies south of Tasmania. *J. Geophys. Res.,* **115,** C04004, doi:10.1029/2008JC005146.

——, and ——, 2011: Subantarctic mode water: Distribution and circulation. *Ocean Dyn.,* **61,** 103–126, doi:10.1007/s10236-010-0352-9.

Hines, K. M., D. H. Bromwich, and G. J. Marshall, 2000: Artificial surface pressure trends in the NCEP–NCAR reanalysis over the Southern Ocean and Antarctica. *J. Climate,* **13,** 3940–3952.

Johnson, G. C., and A. H. Orsi, 1997: Southwest Pacific Ocean water-mass changes between 1968/69 and 1990/91. *J. Climate,* **10,** 306–316.

Kalnay, E., and Coauthors, 1996: The NCEP/NCAR 40-Year Reanalysis Project. *Bull. Amer. Meteor. Soc.,* **77,** 437–471.

King, B., E. Firing, and T. M. Joyce, 2001: Shipboard observations during WOCE. *Ocean Circulation and Climate: Observing and Modelling the Global Ocean,* G. Siedler, Ed., Academic Press, 99–122.

Lefebvre, W., H. Goosse, R. Timmermann, and T. Fichefet, 2004: Influence of the southern annular mode on the sea ice–ocean system. *J. Geophys. Res.,* **109,** C09005, doi:10.1029/2004JC002403.

Levitus, S., J. I. Antonov, T. P. Boyer, and C. Stephens, 2000: Warming of the World Ocean. *Science,* **287,** 2225–2229, doi:10.1126/science.287.5461.2225.

——, ——, ——, R. A. Locarnini, H. E. Garcia, and A. V. Mishonov, 2009: Global ocean heat content 1955–2008 in light of recently revealed instrumentation problems. *Geophys. Res. Lett.,* **36,** L07608, doi:10.1029/2008GL037155.

Lumpkin, R., and K. Speer, 2007: Global ocean meridional overturning. *J. Phys. Oceanogr.,* **37,** 2550–2562.

Marshall, G. J., 2003: Trends in the southern annular mode from observations and reanalyses. *J. Climate,* **16,** 4134–4143.

McCartney, M. S., 1977: Subantarctic Mode Water. *A Voyage of Discovery: George Deacon 70th Anniversary Volume,* M. V. Angel, Ed., Pergamon Press, 103–119.

——, 1982: The subtropical recirculation of mode waters. *J. Mar. Res.,* **40** (Suppl.), 427–464.

McDonagh, E. L., 2009: RRS *James Cook* cruise JC031, 03 Feb-03 Mar 2009. Hydrographic sections of Drake Passage. National Oceanography Centre, Southampton Cruise Rep. 39, 170 pp.

——, H. L. Bryden, B. A. King, R. J. Sanders, S. A. Cunningham, and R. Marsh, 2005: Decadal changes in the south Indian Ocean thermocline. *J. Climate,* **18,** 1575–1590.

Meredith, M. P., K. E. Grose, E. L. McDonagh, K. J. Heywood, R. D. Frew, and P. F. Dennis, 1999: Distribution of oxygen isotopes in the water masses of Drake Passage and the South Atlantic. *J. Geophys. Res.,* **104** (C9), 20 949–20 946.

——, E. J. Murphy, E. J. Hawker, J. C. King, and M. I. Wallace, 2008: On the interannual variability of ocean temperatures around south Georgia, Southern Ocean: Forcing by El Niño/Southern Oscillation and the southern annular mode. *Deep-Sea Res. II,* **55,** 2007–2022, doi:10.1016/j.dsr2.2008.05.020.

Naveira Garabato, A. C., H. Leach, J. T. Allen, R. T. Pollard, and V. H. Strass, 2001: Mesoscale subduction at the Antarctic Polar Front driven by baroclinic instability. *J. Phys. Oceanogr.,* **31,** 2087–2107.

——, L. Jullion, D. P. Stevens, K. J. Heywood, and B. A. King, 2009: Variability of Subantarctic Mode Water and Antarctic Intermediate Water in the Drake Passage during the late-twentieth and early-twenty-first centuries. *J. Climate,* **22,** 3661–3688.

Quartly, G., 2010: RRS James Clark Ross cruise 194, 12–23 Dec 2008. Drake Passage repeat hydrography: WOCE southern repeat section 1b—Burdwood Bank to Elephant Island. National Oceanography Centre, Southampton Cruise Rep. 54, 46 pp.

——, and H. Venables, 2010: RRS *James Clark Ross* cruise 193, 29 Nov–08 Dec 2007. Drake Passage repeat hydrography: WOCE southern repeat section 1b—Burdwood Bank to Elephant Island. National Oceanography Centre, Southampton Cruise Rep. 26, 75 pp.

Rintoul, S. R., and M. H. England, 2002: Ekman transport dominates local air–sea fluxes in driving variability of Subantarctic Mode Water. *J. Phys. Oceanogr.,* **32,** 1308–1321.

Sabine, C. L., and Coauthors, 2004: The oceanic sink for anthropogenic CO_2. *Science,* **305,** 367–371, doi:10.1126/science.1097403.

Saenko, O. A., and A. J. Weaver, 2001: Importance of wind-driven sea ice motion for the formation of Antarctic Intermediate Water in a global climate model. *Geophys. Res. Lett.,* **28,** 4147–4150.

Sallée, J.-B., N. Wienders, K. Speer, and R. Morrow, 2006: Formation of Subantarctic Mode Water in the southeastern Indian Ocean. *Ocean Dyn.,* **56,** 525–542, doi:10.1007/s10236-005-0054-x.

——, K. Speer, S. Rintoul, and S. Wijffels, 2010: Southern Ocean thermocline ventilation. *J. Phys. Oceanogr.,* **40,** 509–529.

Santoso, A., and M. H. England, 2004: Antarctic Intermediate Water circulation and variability in a coupled climate model. *J. Phys. Oceanogr.,* **34,** 2160–2179.

Sarmiento, J. L., N. Gruber, M. A. Brzezinski, and J. P. Dunne, 2004: High-latitude controls of thermocline nutrients and low latitude biological productivity. *Nature,* **427,** 56–60, doi:10.1038/nature02127.

Schneider, W., M. Fukasawa, H. Uchida, T. Kawano, I. Kaneko, and R. Fuenzalida, 2005: Observed property changes in eastern South Pacific Antarctic Intermediate Water. *Geophys. Res. Lett.,* **32,** L14602, doi:10.1029/2005GL022801.

Simmonds, I., and J. C. King, 2004: Global and hemispheric climate variations affecting the Southern Ocean. *Antarct. Sci.,* **16,** 401–413, doi:10.1017/S0954102004002226.

Sloyan, B. M., and S. R. Rintoul, 2001: The Southern Ocean limb of the global deep overturning circulation. *J. Phys. Oceanogr.,* **31,** 143–173.

Smith, C. A., and P. D. Sardeshmukh, 2000: The effect of ENSO on the intraseasonal variance of surface temperatures in winter. *Int. J. Climatol.,* **20,** 1543–1557.

Sokolov, S., and S. R. Rintoul, 2002: Structure of Southern Ocean fronts at 140°E. *J. Mar. Syst.,* **37,** 151–184, doi:10.1016/S0924-7963(02)00200-2.

——, and ——, 2009: Circumpolar structure and distribution of the Antarctic Circumpolar Current fronts: 2. Variability and relationship to sea surface height. *J. Geophys. Res.,* **114,** C11019, doi:10.1029/2008JC005248.

Sparrow, M., and E. Hawker, 2005: RRS *James Clark Ross* cruise 115, 01 Dec–19 Dec 2004. Drake Passage repeat hydrography: WOCE southern repeat section 1b—Burdwood Bank to Elephant Island. Southampton Oceanography Centre Cruise Rep. 56, 80 pp.

Stansfield, K., and M. Meredith, 2008: RRS *James Clark Ross* cruise 139, 05 Dec–12 Dec 2005. Drake Passage repeat hydrography: WOCE southern repeat section 1b—Burdwood Bank to Elephant Island. National Oceanography Centre, Southampton Cruise Rep. 24, 72 pp.

Sun, C., and D. R. Watts, 2001: A circumpolar gravest empirical mode for the Southern Ocean hydrography. *J. Geophys. Res.,* **106,** 2833–2855.

Talley, L. D., 1996: Antarctic Intermediate Water in the South Atlantic. *The South Atlantic: Present and Past Circulation,* G. Wefer et al., Eds., Springer-Verlag, 219–238.

Thompson, D. W. J., and S. Solomon, 2002: Interpretation of recent Southern Hemisphere climate change. *Science,* **296,** 895–899, doi:10.1126/science.1069270.

——, ——, P. J. Kushner, M. H. England, K. M. Grise, and D. J. Karoly, 2011: Signatures of the Antarctic ozone hole in Southern Hemisphere surface climate change. *Nat. Geosci.,* **4,** 741–749, doi:10.1038/ngeo1296.

Timmermann, R., A. Worby, H. Goosse, and T. Fichefet, 2004: Utilizing the ASPeCt sea ice thickness data set to evaluate a global coupled sea ice–ocean model. *J. Geophys. Res.,* **109,** C07017, doi:10.1029/2003JC002242.

Turner, J., and Coauthors, 2009: Non-annular atmospheric circulation change induced by stratospheric ozone depletion and its role in the recent increase of Antarctic sea ice extent. *Geophys. Res. Lett.,* **36,** L08502, doi:10.1029/2009GL037524.

Verdy, A., J. Marshall, and A. Czaja, 2006: Sea Surface temperature variability along the path of the Antarctic Circumpolar Current. *J. Phys. Oceanogr.,* **36,** 1317–1331.

von Schuckmann, K., F. Gaillard, and P.-Y. Le Traon, 2009: Global hydrographic variability patterns during 2003–2008. *J. Geophys. Res.,* **114,** C09007, doi:10.1029/2008jc005237.

Watanabe, T., M. Ikeda, and M. Wakatsuchi, 2004: Thermohaline effects of the seasonal sea ice cover in the Sea of Okhotsk. *J. Geophys. Res.,* **109,** C09S02, doi:10.1029/2003JC001905.

Williams, A., R. Hadfield, and G. Quartly, 2008: RRS *James Clark Ross* cruise 163, 07 Dec–15 Dec 2006. Drake Passage repeat hydrography: WOCE southern repeat section 1b—Burdwood Bank to Elephant Island. National Oceanography Centre, Southampton Cruise Rep. 25, 64 pp.

Wong, A., A. Bindoff, and J. Church, 1999: Large-scale freshening of intermediate waters in the Pacific and Indian Oceans. *Nature,* **400,** 440–443, doi:10.1038/22733.

——, ——, and ——, 2001: Freshwater and heat changes in the North and South Pacific Oceans between the 1960s and 1985–94. *J. Climate,* **14,** 1613–1633.

Yuan, X., and C. Li, 2008: Climate modes in southern high latitudes and their impacts on Antarctic sea ice. *J. Geophys. Res.,* **113,** C06S91, doi:10.1029/2006JC004067.